



PONTIFICIA UNIVERSIDAD CATÓLICA DE CHILE
FACULTAD DE FÍSICA
INSTITUTO DE FÍSICA

*Magneto-Thermal Evolution of Neutron Star
Cores in the “Strong-Coupling Regime”*

by

Nicolás Andrés Moraga Vent

Thesis submitted to the Faculty of Physics
of Pontificia Universidad Católica de Chile, as one of the requirements
to qualify for the academic Master’s degree in Physics.

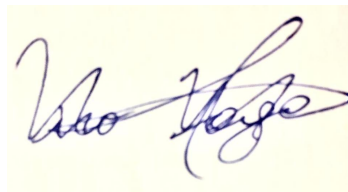
Supervisor : Dr. Andreas Reisenegger
Co-supervisor : Dr. Francisco Castillo
Dr. Juan Alejandro Valdivia
Committee : Dr. Felipe Veloso
: Dr. Rafael Benguria

December, 2020
Santiago, Chile

©2020, Nicolás Moraga Vent.

Authorization for the Reproduction of the Thesis

I, Nicolás Moraga, declare that this thesis titled, “Magneto-Thermal Evolution of Neutron Star Cores in the Strong-Coupling Regime ” and the work presented in it are authorized for partial or total reproduction, with academic ends, by any means or procedure, including a bibliographical cite that accredit the work and its author.

A handwritten signature in blue ink on a yellow rectangular background. The signature is cursive and appears to read 'Nicolás Moraga'.

Signed

12/01/2020

Date

“We are all in the gutter, but some of us are looking at the stars”

Oscar Wilde.

A mis padres

Abstract

In the previous works of [Castillo et al. 2017](#) and [Castillo et al. 2020](#), the first simulations of ambipolar diffusion in spherical neutron star cores were reported, contributing to the understanding of the long-term evolution of their magnetic fields. These contributions, however, did not consider the effects of the temperature evolution of the neutron star interior, and the impact of β -decays (Urca reactions) in the magnetic evolution. The purpose of this M.Sc.-thesis is to include these two effects. We focus on a young neutron star, with internal temperatures about $T \gtrsim 10^9$ K, where the particles in the core (assumed to be mainly electron, protons, and neutrons) are strongly coupled by collisional forces and can convert into each other by Urca reactions, in the so called “strong-coupling regime“. At this stage, the magnetic field induces small fluid displacements, changing the local chemical composition and generating pressure gradient forces, which tend to be erased by Urca reactions. Depending on the strength of the chemical departure, this reactions can lead to a non-trivial thermal evolution as a consequence of the magnetic feedback, which can even produce a net heating of the core. This mechanism converts magnetic to thermal energy and could explain the high surface luminosity in newly born magnetars (highly magnetize neutron stars). In this thesis, we present the first long-term magneto-thermal simulation of a neutron star core in this regime. We found that the magnetic field evolves towards barotropic “Grad-Shafranov equilibria”, in which the magnetic force is mostly balanced by the degeneracy pressure gradient and gravitational force of neutrons. We concluded that, for internal magnetic field strength field $B \gtrsim 10^{16}$ G, a non-trivial thermal evolution due to non-equilibrium Urca reactions is not possible because it would occur at a late state, when the ambipolar heating (due to the diffusion of charged particles through neutrons) is more likely to heat the core.

Agradecimientos

Quisiera agradecer a mis padres, Lorenzo y Mónica, por su incondicional apoyo y amor, y por haberme dado la mejor educación que pudieron. A mis hermanos, Camila y Álvaro, les agradezco también todo su apoyo y amor durante estos años. A mis amigos, Katherine, Jacobo, Tamara, Daniel, María José, Marcelo y Gisella, por mantenerme cuerdo y con buen humor, y por todos los inolvidables momentos que hemos vivido, en particular, por el apoyo y motivación que siempre me brindaron durante estos años de estudio.

Agradezco a mis tutores, Andreas Reisenegger, Francisco Castillo y Alejandro Valdivia, por su disponibilidad, experiencia y preocupación constante por mi trabajo. Un distinguido agradecimiento a Francisco Castillo por su paciencia y buena voluntad durante este trabajo. Agradezco a los miembros del grupo ANSWERS por las valiosas discusiones y recomendaciones realizadas para este trabajo. También quiero agradecer al Prof. Guillermo Palma del Dpto. de Física de la Universidad de Santiago de Chile, por su apoyo en momentos difíciles durante mi pregrado y por su constante motivación en estos últimos años.

Agradezco también a los miembros de esta comisión por aceptar ser parte de ella, y por su apoyo a este trabajo de tesis. Agradezco a las fuentes de financiamiento FONDECYT regular 1171421, 1201582 y FONDECYT postdoctorado 3180700.

Contents

1	Introduction	9
1.1	Structure	9
1.2	Classes of NSs	10
1.3	Magnetic fields	11
1.3.1	Magnetic field measurement	11
1.3.2	$P\dot{P}$ -diagram	12
1.3.3	Origin of the magnetic field	12
1.4	Magnetic evolution	14
1.4.1	Hall drift and Ohmic dissipation	14
1.4.2	Ambipolar diffusion	15
1.4.3	Urca reactions	15
1.5	Internal temperature evolution	16
2	Physical Model	19
2.1	Evolution of the magnetic field	20
2.1.1	Background NS model	22
2.1.2	Linearization	23
2.2	Boundary conditions	25
2.3	Axially symmetric fields	25
2.4	Energy Dissipation	25
2.4.1	Energy stored in the density perturbations	26
2.4.2	Energy stored by the magnetic field	26
2.5	Temperature evolution	28
2.5.1	Heat capacity	28
2.5.2	Neutrino luminosity	28
2.6	Strong and weak-coupling regimes	30
2.6.1	Strong Coupling	31
2.6.2	Weak Coupling	32
2.7	Time-scales	32
2.7.1	Short-term relaxation through fictitious friction	33
2.7.2	Long-term evolution through mUrca reactions	34

3	Numerical approach	37
3.1	Time parametrization	37
3.2	Dimensionless equations	39
4	Results	43
4.1	Constant temperature	44
4.1.1	Dependence on the artificial friction	44
4.1.2	Hydro-magnetic and magneto-chemical evolution	46
4.1.3	Force balance and continuity equations	48
4.1.4	Energy dissipation	51
4.1.5	Grad-Shafranov equilibria	53
4.2	Temperature evolution	55
4.2.1	Dependence on the artificial friction	55
4.2.2	Magnetic field scaling	60
4.2.3	Magnetic feedback	60
5	Conclusion	65

List of Figures

1.1	Internal structure of a neutron star	10
1.2	$P-\dot{P}$ diagram showing the distribution of 1980 NSs as a function of their period and period derivative, some of which have an associated supernova remnant (SNR), including 3 central Compact Objects (CCOs), 22 magnetars, 7 isolated neutron stars (XINs) and 151 objects in binary systems, 39 of whom are in globular clusters. The figure also includes lines of constant magnetic field, characteristic age, and spin-down luminosity. Plot by C. Espinoza, from the ATNF Pulsar catalog https://www.atnf.csiro.au/research/pulsar/psrcat/	13
2.1	Function $M_M(\xi)$ and its approximation $M_{app}(\xi)$ in the sub-thermal case given by equations (2.63) and (2.64).	30
3.1	Spherical grid used to spatially discretize the code variables.	40
4.1	Comparison of the evolution of simulations using the same initial condition, equations (4.1) to (4.4), at constant temperature $T = 3 \times 10^9 \text{K}$, and three very different values of ζ (10^{-3} , red; 10^{-4} , blue, and 10^{-5} , black), with the following ratios between the different relevant time-scales at the center of the star; $t'_{\zeta p} : t'_{\zeta g} : t'_{\zeta B} : t'_{\lambda B} = 1 : 16.5 : 548 : 12038$, $t'_{\zeta p} : t'_{\zeta g} : t'_{\zeta B} : t'_{\lambda B} = 1 : 16.5 : 548 : 120384$ and $t'_{\zeta p} : t'_{\zeta g} : t'_{\zeta B} : t'_{\lambda B} = 1 : 16.5 : 548 : 1203840$, respectively. The vertical lines show the values of all the time-scales with their respective color for the different ζ of each simulation. We used a grid of $N_r = 60$ radial steps and $N_\theta = 91$ polar steps inside the core, as well as $N_{Exp} = 27$ external multipoles. The panels show the time evolution of: (a) the magnetic field $\langle \mathbf{B} \rangle$ in units of B_0 , (b) the poloidal component of the fluid velocity $\langle \mathbf{v}_{pol} \rangle$, and (c) chemical imbalance $\langle \Delta\mu \rangle$. Here, $\langle \cdot \rangle$ denotes the root mean square (rms) average in the volume of the core.	45

- 4.2 Evolution of the magnetic field for the simulation shown in Fig. 4.1 with $\zeta = 10^{-4}$. From left to right: (a) Configuration of the magnetic field, where lines represent the poloidal magnetic field (labeled by the magnitude of α) and colors the toroidal potential β ; (b) and (c) the fractional density perturbations $\delta n_c/n_c$ and $\delta n_n/n_n$, respectively; (d) the poloidal component of the velocity field, \mathbf{v} , normalized to R/t_0 and (e) net emission rate in units of $\lambda_0\mu_0$. Rows correspond to different times: $t' = 0, t'_{\zeta p}, t'_{\zeta g}, t'_{\zeta B}$, and $t'_{\lambda B}$ 47
- 4.3 Time evolution of the force balance for the simulation with $\zeta = 10^{-4}$ in Fig. 4.1: $\langle \mathbf{f}_B^{\text{Pol}} \rangle$, $\langle \mathbf{f}_B^{\text{Tor}} \rangle$, $\langle \mathbf{f}_n \rangle$, $\langle \mathbf{f}_c \rangle$, and $\langle \mathbf{f}_\zeta^{\text{Pol}} \rangle$ normalized to $\langle \mathbf{f}_B^{\text{Pol}}(t=0) \rangle$, where $\langle \cdot \rangle$ denotes the rms average over the NS volume. The vertical lines show, from left to right, the values of the time-scales $t'_{\zeta p}$, $t'_{\zeta g}$, $t'_{\zeta B}$ and $t'_{\lambda B}$ 48
- 4.4 Terms of the continuity equations for the simulation with $\zeta = 10^{-4}$; (a) shows the time evolution of the quotient $\langle \nabla \cdot (n_c \mathbf{v}') \rangle / \langle \nabla \cdot (n_n \mathbf{v}') \rangle$, (b) shows the quotient of $\langle \partial \delta n_n / \partial t' \rangle / \langle \nabla \cdot (n_n \mathbf{v}') \rangle$ (dashed) and $\langle \partial \delta n_c / \partial t' \rangle / \langle \nabla \cdot (n_c \mathbf{v}') \rangle$ (solid), (c) shows $\langle \partial \delta n_n / \partial t' \rangle / \langle \lambda \Delta \mu \rangle$ (dashed) and $\langle \partial \delta n_c / \partial t' \rangle / \langle \lambda \Delta \mu \rangle$ (solid), and (d) shows the quotient $\langle v'_{\text{pol}} \rangle / \langle \lambda \Delta \mu \rangle$, where $\langle \cdot \rangle$ denotes the rms average over the NS core. The vertical lines show, from left to right, the values of the time-scales $t'_{\zeta p}$, $t'_{\zeta g}$, $t'_{\zeta B}$ and $t'_{\lambda B}$ 50
- 4.5 Magnetic energy dissipation; (a) for the simulation with $\zeta = 10^{-4}$ in Fig. 4.1; each term in the equation (2.48) multiplied by time and normalized to the maximum value of $\dot{E}'_B t'$. In pink the time derivative of the magnetic energy, in blue the Poynting flux, in green the dissipation by the artificial friction force, in red the chemical energy released, and in black the internal energy enhancement. (b) for the simulations with $\zeta = 10^{-4}$ (black), and $\zeta = 10^{-3}$ (blue) in Fig. 4.1; $\mathcal{L}'_{\zeta}{}^{\text{Tor}} t'$ (dash-dotted), $\mathcal{L}'_{\zeta}{}^{\text{Pol}} t'$ (dashed) and $\mathcal{L}'_{\text{HV}} t'$ (solid). The vertical lines show in (a), from left to right, the values of the time-scales $t'_{\zeta p}$, $t'_{\zeta g}$, $t'_{\zeta B}$ and $t'_{\lambda B}$, respectively; and in (b) only the time-scales $t'_{\zeta B}$, and $t'_{\lambda B}$ with their respective color. 52
- 4.6 For the simulation with $\zeta = 10^{-4}$: Scatter plot of α versus (a) β , (b) χ_n , and (c) χ_c . In (d) χ_c versus χ_n , in the last figure we plot the identity function in black. We show the relation at all the grid points at $t' = 0, t'_{\zeta p}, t'_{\zeta g}, t'_{\zeta B}, 10t'_{\zeta B}$, and $t'_{\lambda B}$, respectively. 54
- 4.7 Time evolution of the ‘‘Grad-Shafranov integral’’ I_{GS} (defined in equation [4.10]). The vertical lines show, from left to right, the values of the time-scales $t'_{\zeta p}$, $t'_{\zeta g}$, $t'_{\zeta B}$, and $t'_{\lambda B}$ 55

- 4.8 Thermal evolution: The upper panels show the luminosities for the artificial friction dissipation \mathcal{L}_ζ (green), chemical energy released $\mathcal{L}_{H\nu}$ (blue), and equilibrium neutrino luminosity \mathcal{L}_ν^* (black), normalized to the initial value $\mathcal{L}_\nu^*(t = 0)$. Panel (a) corresponds to the thermal evolution for the simulation discussed in Sec. 4.1.5, where the initial temperature is $T_0 = 3 \times 10^9$ K. Panels (b) and (c) correspond to the simulations with $T_0 = 3 \times 10^{10}$ K, and $T_0 = 10^{11}$ K, with different values of $\zeta(T_0)$ ($10^{-4} \times [3 \times 10^{10} / 3 \times 10^9]^{-6} = 10^{-10}$ and $10^{-4} \times [10^{11} / 3 \times 10^9]^{-6} = 7.3 \times 10^{-14}$, respectively). Panel (d) shows the evolution of temperature, normalized to T_0 , for each of the former values; the pink curve corresponds to the results shown in panel (a), the blue curve to panel (b), and the black curve to panel (c). For all these simulations, the magnetic field strength was the same $B \approx 3 \times 10^{17}$ G ($b^2 = 0.03$). The vertical lines show, from left to right, the values of the time-scales $t_{\zeta p}$, $t_{\zeta g}$, $t_{\zeta B}$, t_λ , and $t_{\lambda B}$, obtained from equation (3.9). 58
- 4.9 Time variable comparison between the constant-temperature variable t' and the variable-temperature time variable t . The curves correspond to the same simulations shown in Fig. 4.8: In pink, the results in panel (a) (pink curve also in panel (d)); in blue, the results in panels (b) (blue curve also in panel (d)); and in black the results in panels (c) (black curve also in panel (d)), and (f). The horizontal lines, for each color and from bottom to top, correspond to the time-scales $t_{\zeta p}$, $t_{\zeta g}$, $t_{\zeta B}$, t_λ , and $t_{\lambda B}$ (obtained from equation [3.9]), with their respective colors. The vertical lines, for each color and from left to right, correspond to $t'_{\zeta p}$, $t'_{\zeta g}$, $t'_{\zeta B}$, t'_λ and $t'_{\lambda B}$ 59
- 4.10 Magnetic field scaling: The upper panels, (a) and (b), show the curves for the chemical energy released $\mathcal{L}_{H\nu}$, and the artificial friction dissipation \mathcal{L}_ζ after evolving temperature with $T_0 = 10^{11}$ K, and three different values of b^2 (0.01, pink; 0.02, black; and 0.03, blue). The lower panels (c) and (d), show the same curves after applying the scaling in equation (4.12), to the results with $b^2 = 0.02$ and 0.03, to obtain the results with $b^2 = 0.01$. The vertical lines correspond, from left to right, t_λ and $t_{\lambda B}$ (with their respective colors in the upper panels), obtained from equation (3.9). 61

- 4.11 Magneto-thermal evolution: In panel (a), the evolution of temperature with $T_0 = 10^{11}$ K, and the horizontal line corresponds to $T_{eq} = 5 \times 10^8$ K (defined in equation [2.69]), where the transition to the weak-coupling regime occurs and the present approach ceases to be valid. Panel (b) shows the equilibrium neutrino luminosity \mathcal{L}_ν^* (black), chemical energy released $\mathcal{L}_{H\nu}$ (blue), and the artificial friction dissipation \mathcal{L}_ζ (green). Panel (c) shows the evolution of $\langle \xi \rangle$ (black), and $\sqrt{\mathcal{L}_{H\nu}/\mathcal{L}_\nu^*}$ (cyan), where $\langle \cdot \rangle$ denotes root mean square (rms) average in the volume of the core. The vertical lines correspond, from left to right, to t_λ and $t_{\lambda B}$, obtained from equation (3.9). Here the magnetic field strength has been scaled, using equation (4.12), from $B \approx 3 \times 10^{17}$ G ($b^2 = 0.03$) to $B \approx 8 \times 10^{16}$ G ($b^2 = 0.002$). 63

Chapter 1

Introduction

Neutron stars (NSs) are compact stars, remnants of supernova explosions of old massive stars. Historically, it was first Landau in 1931 (published in 1932) whom speculated about the existence of stars more compact than white dwarfs. Although, neutrons were discovered one year later by Chadwick (1932), and Landau's arguments were questionable. The existence of NSs was predicted later by Baade & Zwicky (1934), who proposed an explanation for the enormous energy release in these supernova explosions, which was confirmed for the first time 30 years later by Hewish et al. (1968). The most extreme astrophysical conditions are met in NSs; they are extremely dense objects with masses around $\sim 1.4 M_{\odot}$ in a radius of 12 km, central densities about 10^{15}g cm^{-3} (higher than the nuclear saturation density $\rho_0 = 2.4 \times 10^{14} \text{g cm}^{-3}$), surface gravitational accelerations about 10^{14}cm s^{-2} and the largest magnetic fields in universe, about $B \sim 10^{11-13} \text{G}$ for the typical surface field in pulsars (Manchester et al., 2005), and even $B \lesssim 10^{14} \text{G}$, and $B \lesssim 10^{15} \text{G}$ in radio pulsars and magnetars. In their interior self-gravity is balanced by a pressure gradient of highly degenerate fermions, mostly neutrons, but with presence of protons, electrons, and other species at increasing densities, as we approach their center.

1.1 Structure

After the discovery of pulsars, a vast theoretical and observational progress has taken place. Nowadays, the NS structure is understood as shown in Fig. 1.1:

- *Atmosphere*: It consists of a thin layer of plasma, whose thickness varies from some ten centimeters in a hot neutron star, with surface temperature about $T_s \sim 3 \times 10^6 \text{K}$, to some few millimeters in a cold one where $T_s \sim 3 \times 10^5 \text{K}$. The spectrum of thermal electromagnetic neutron star radiation is formed in this region.
- *Outer crust*: This region extends from the bottom of the atmosphere, with densities $\sim 10^6 \text{g cm}^{-3}$, to some hundreds meters where densities become

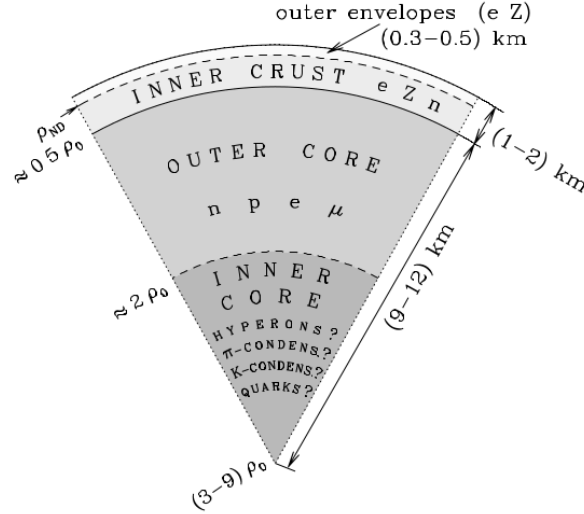


Figure 1.1: Internal structure of a neutron star

$\sim 4 \times 10^{11} \text{g cm}^{-3}$. It is composed mainly of a lattice of heavy ions (high Z) and free electrons e .

- *Inner crust:* The extension of this region may be about one kilometer thick. Here, heavy ions coexist with a neutron fluid (some of which may be in a superfluid state and is expected to play a crucial role in pulsar glitches (Baym et al., 1969)).
- *Outer core:* The outer core is several kilometers thick, with densities that vary from 2×10^{14} to $\sim 10^{15} \text{g cm}^{-3}$. At those densities, matter is believed to consist mainly of a fluid of highly degenerate neutrons n , with a small fraction of protons p (which may be in a superfluid/superconducting state, respectively), relativistic electrons e and muons μ ($npe\mu$ -matter composition).
- *Inner core:* In this region of several kilometers, at densities about $\rho \gtrsim 10^{15} \text{g cm}^{-3}$, the structure and composition of NSs matter becomes more uncertain. It might be a fluid composed of exotic particles like mesons, hyperons, free quarks, or others.

1.2 Classes of NSs

According to the current observational knowledge, there are several classes of NSs depending on their inferred magnetic field strength and rotational period:

Isolated neutron stars (INSs): This class of NSs have characteristic ages of 1-4 Myr and magnetic fields about $1-3 \times 10^{13} \text{G}$ (Kaplan & Van Kerkwijk, 2005,

2009), they also present a quasi-thermal X-ray spectrum with low luminosity and relatively long period 3-11 s. It is expected that their X-ray spectrum is not contaminated by effects from its magnetosphere, so they are potentially useful to restrict the unknown equation of state of dense matter ($\rho > \rho_0$) (Kaspi, 2010).

Rotation-powered pulsars (RPPs) (also known simply as Radio pulsars): are characterized by periodic pulsations in frequency observable more easily in the radio band and with magnetic fields about 10^8 G to 9×10^{13} G, and periods about 1.5 ms to 12 s (Kaspi, 2010).

High-B rotation-powered pulsars (high-B RPPs): These pulsars have high estimated magnetic fields $B \geq 10^{13}$ G and show X-ray properties which are consistent with spectra of transient magnetars in quiescence (Kaspi & McLaughlin, 2004).

Rotating radio transients (RRATs): McLaughlin et al. (2006) discovered brief radio bursts from Galactic sources, but with no directly observed radio periodicities. It was first thought that RRATs were a new class of NSs, but now it seems that they are most likely an extreme case of RPPs (Weltevrede et al., 2006). Their discovery is important since it suggests that there are a lot of NSs that have not been detected by radio telescopes that look for them based on the periodicity of their radiation (McLaughlin et al., 2006; Keane & Kramer, 2008).

Central compact objects (CCOs): these are young NSs, with ages $\lesssim 10^4$ yr, at the centre of supernova explosion remnants. These objects are detected through their thermal X-ray emission and their properties have prevented their classification as one of the other classes. (Ho, 2012; Kaspi, 2010; Pavlov & Luna, 2009; Mereghetti et al., 2002; Chakrabarty et al., 2001)

Magnetars: Magnetars are young and highly magnetized NSs with ultra strong magnetic field strengths about 10^{14-15} G and long periods $P \sim 2 - 12$ s. They present wide range of X-ray activity powered by their magnetic field decay (Duncan & Thompson, 1992; Thompson & Duncan, 1993, 1995, 1996) including quasi-periodic oscillations, glitches and anti-glitches, and giant flares emitting huge amounts of energy (10^{40-46} erg in periods about seconds to minutes). Also, as a consequence of the ultra strong magnetic field, QED effects such as vacuum polarization or photon splitting can occur, since the magnetic field is well above the critical field $B_{QED} \equiv m_e^2 c^3 / \hbar e = 4.4 \times 10^{13}$ G.

1.3 Magnetic fields

1.3.1 Magnetic field measurement

The slowly decreasing frequency of the observed electromagnetic radiation from NSs, is believed to be caused by the decrease of the rotational frequency Ω of the star. The star's spin-down is modeled in terms of a magnetic dipole rotating in vacuum, and the lost magnetic energy is given by

$$I\Omega\dot{\Omega} \propto -\mu_{NS}^2 \Omega^4, \quad (1.1)$$

where the dot represents a time derivative, I is the star’s moment of inertia, and μ_{NS} is its magnetic dipole moment. This allows to estimate the magnitude of the dipolar component of the magnetic field at the surface of the star as

$$B = 3.2 \times 10^{19} \left(P \dot{P} \right)^{1/2} \text{ G}, \quad (1.2)$$

where $P = 2\pi/\Omega$ is the rotation period of the star expressed in seconds. This model also allows to provide a characteristic spin-down time as an estimation of the age of the star, which is given by

$$\tau = \frac{P}{2\dot{P}}. \quad (1.3)$$

1.3.2 $P\dot{P}$ -diagram

In Fig. 1.2, we show the $P\dot{P}$ diagram, which provides information about the population of NSs and their properties in terms of the observables P and \dot{P} . From here, one may obtain the characteristic ages τ , and surface magnetic field strength B from the equations (1.2) and (1.3). The $P\dot{P}$ diagram is also useful for following the lives of different classes of NSs. For example, in the upper middle of the diagram are located the young NSs associated with supernova remnants (SNRs). They slow down and evolve over millions of years to become one of the large population of $P \sim 1$ s “slow” pulsars, in the middle of the diagram, until their rate of rotation is too slow to power the radio emission mechanism, disappearing from view.

1.3.3 Origin of the magnetic field

The origin of the strong magnetic fields of NSs is not well understood yet. However, the maximum magnetic flux for upper main sequence stars, white dwarf, and neutrons stars seems to be similar (Reisenegger, 2009), namely

$$\Phi_{max} = \pi R^2 B_{max} \sim 10^{27.5} \text{ G cm}^{-2}, \quad (1.4)$$

here R is the stellar radius and B_{max} is the maximum magnetic field, suggesting that the strong magnetic fields found in NSs may have a “fossil” origin due to flux freezing during the stellar collapse. In fact, this corresponds to the prediction of magnetars originally made by Woltjer (1964). However, following the flux freezing hypothesis, B should be much smaller because only the central volume ($\sim 0.2\%$) of the progenitor collapses to form a proto-neutron star (Mereghetti et al., 2015). Following flux compression, an amplification of the magnetic field in the proto-neutron star by dynamo action driven by convection and differential rotation is expected (Duncan & Thompson, 1992; Thompson & Duncan, 1993; Bonanno et al., 2005; Braithwaite, 2006). However, magnetic flux would tend to escape buoyantly from the dynamo region (Spruit, 2009; Gusakov & Kantor, 2013).

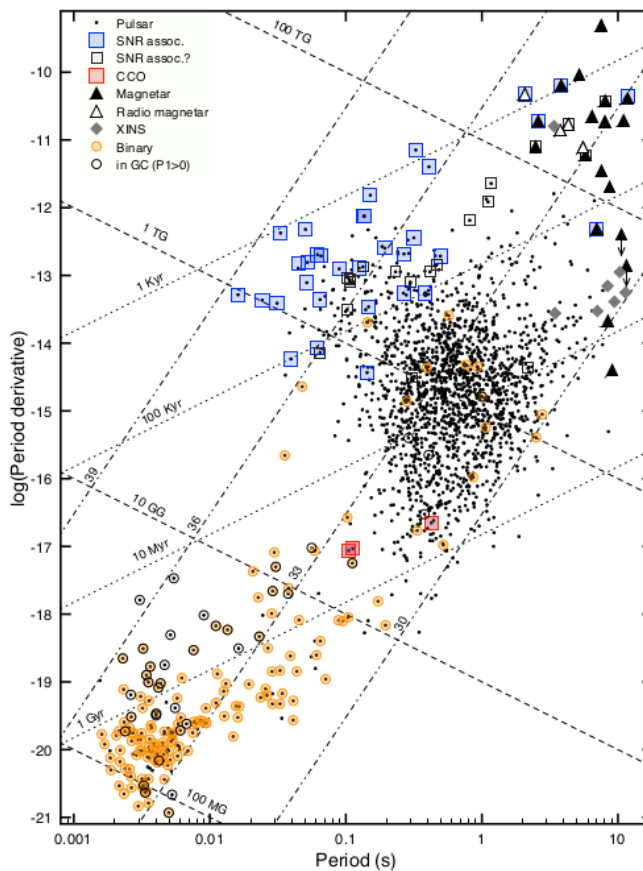


Figure 1.2: $P-\dot{P}$ diagram showing the distribution of 1980 NSs as a function of their period and period derivative, some of which have an associated supernova remnant (SNR), including 3 central Compact Objects (CCOs), 22 magnetars, 7 isolated neutron stars (XINSs) and 151 objects in binary systems, 39 of whom are in globular clusters. The figure also includes lines of constant magnetic field, characteristic age, and spin-down luminosity. Plot by C. Espinoza, from the ATNF Pulsar catalog <https://www.atnf.csiro.au/research/pulsar/psrcat/>.

1.4 Magnetic evolution

As we have already discussed, there is an evident difference in the magnetic field strength among all the different classes of NSs, depending on their evolution. Hence, understanding the long-term magneto-thermal evolution in NSs interiors is crucial to understand the relation between these kinds of objects and their observational properties. To exemplify the evidence of magnetic field evolution and its observational implications, we may consider magnetars for example. They have been observed as anomalous X-ray pulsars and soft gamma repeaters, with typical surface luminosities $\mathcal{L}_s \sim 10^{35} \text{erg s}^{-1}$ (Durant & van Kerkwijk, 2006; Olausen & Kaspi, 2014) and associated surface temperature of about $T_s \approx 4 \times 10^6 \text{K}$ ¹. However, it is expected that most of their thermal energy should be quickly lost due to neutrino emission and, for a 1 kyr-old NS, its surface temperature should become $T_s \sim 10^6 \text{K}$, with an associated surface luminosity $\mathcal{L}_s \sim 10^{33} \text{erg s}^{-1}$ (Yakovlev & Pethick, 2004a). On the other hand, these objects appear to be isolated and their spin-down luminosity (rate of rotational energy loss) is about $\mathcal{L}_{rot} \sim 4\pi^2 I \dot{P} / P^3 \sim 10^{33} \text{erg s}^{-1}$ (Rea, 2014). Therefore, their strong activity can only be explained in terms of a decaying magnetic field, which must be attributed to processes intrinsic to the NSs (Thompson & Duncan, 1995, 1996). Before starting with the analysis of these processes, we remark that the mechanisms that generate the magnetic field evolution in the crust are substantially different than those in the core: In the solid crust, ions have very restricted mobility and currents are carried by electrons. In the core, however, the species are in a fluid state whose radial composition gradients (due to the different density profiles of charged particles and neutrons) stably stratified the fluid, i.e. strong buoyancy forces oppose convective motions (Pethick, 1992; Goldreich & Reisenegger, 1992). Thus, for any physical process to evolve the magnetic field in the core, it must erode the stable stratification.

The processes that evolve the magnetic field in a non-superfluid star are the following:

1.4.1 Hall drift and Ohmic dissipation

Hall drift is the advection of magnetic field lines by the electric current generated by the flow of the electron fluid relative to the ions and Ohmic diffusion is a dissipative effect caused by electric resistivity, which depends on a very uncertain “impurity parameter” (Cumming et al., 2004). Though Hall drift does not contribute to the dissipation of magnetic energy, it can generate new electric currents, and when Ohmic dissipation is taken into account the evolution may lead to a steady state (Gourgouliatos & Cumming, 2014). These effects in the NS core are substantially slower because the density and conductivity are higher than those of the crust and proceed in time-scales given by (Goldreich &

¹For more characteristic values of \mathcal{L}_s , see the online McGill magnetar catalog, <http://www.physics.mcgill.ca/pulsar/magnetar/main.html>.

Reisenegger, 1992)

$$t_{\text{Hall}} \sim 5 \times 10^5 \left(\frac{10^{15} \text{G}}{B} \right)^{-1} \left(\frac{L}{1 \text{km}} \right)^2 \left(\frac{\rho}{\rho_0} \right) \text{yr}, \quad (1.5)$$

$$t_{\text{Ohm}} \sim 2 \times 10^{11} \left(\frac{T}{10^8 \text{K}} \right)^{-2} \left(\frac{L}{1 \text{km}} \right)^2 \left(\frac{\rho}{\rho_0} \right)^3 \text{yr}. \quad (1.6)$$

1.4.2 Ambipolar diffusion

Ambipolar diffusion is the motion of charged particles (coupled with the magnetic field) with respect to the neutron fluid in the core, controlled by the force due to collisions between particles of these two fluids. Recently, the first simulations of ambipolar diffusion in a spherical star were reported, first for charged particles moving through a static neutron background (Castillo et al., 2017), and then in a two-fluid simulation where the neutron motion was taken into account (Castillo et al., 2020). It was concluded that the neutron motion can reduce the time-scale at which ambipolar diffusion operates, namely

$$t_{\text{ad}} \sim (0.3 - 3) \times 10^3 \left(\frac{10^{15} \text{G}}{B} \right)^2 \left(\frac{T}{10^8 \text{K}} \right)^2 \left(\frac{L}{1 \text{km}} \right)^2 \text{yr}, \quad (1.7)$$

where L is the typical spatial scale of the magnetic field, as also found by Ofengeim & Gusakov (2018).

This mechanism has been historically invoked to explain the activity of magnetars due to its strong dependence on the magnetic field intensity (Thompson & Duncan, 1995, 1996). More recently Beloborodov & Li (2016) concluded that ambipolar diffusion could explain the high X-ray luminosity for a brief period $< 1 \text{kyr}$. However, this is feasible only for ultra-strong magnetic fields $B \gtrsim 10^{16} \text{G}$. Ambipolar diffusion has also been suggested to explain the low magnetic fields of millisecond pulsars, as the collisional coupling between charged particles and neutrons decreases at low temperatures, so the time-scale of ambipolar diffusion may become short enough to predict substantial magnetic field decay in old neutron stars prior to their spin up by accretion (Cruces et al., 2019).

1.4.3 Urca reactions

After the supernova explosion, a proto-NS is born in an extremely hot and liquid state, with a temperature $T \gtrsim 10^{10} \text{K}$, and still opaque to neutrinos. At this stage, thermal effects and neutrino reabsorption constitute a relevant energy source. However, within a minute, the star becomes neutrino-transparent and the young NS is formed (Burrows & Lattimer, 1986; Keil & Janka, 1995; Pons et al., 1999). In the following early life of the NS, the highly frequent proton-neutron collisions strongly couple the different plasma species, due to β -decays, the so-called ‘‘Urca reactions’’ (for historical footnote see Shapiro & Teukolsky 1983), the species can convert into each other emitting neutrinos

that take away most of the thermal energy. Therefore, the magnetic field must evolve in such a way that the Lorentz force balances the fluid pressure forces that change due to the particle conversion. Nevertheless, in this case the time-scale at which this process operates depends on the particular neutrino emission process. Among them, the most powerful is the direct β -decay, usually called “direct Urca process” (dUrca),



However, since the neutron star interior is composed of highly degenerate matter, the condition

$$|p_{Fp} - p_{Fe}| \leq p_{Fn} \leq p_{Fp} + p_{Fe}, \tag{1.9}$$

where p_{Fi} is the Fermi momentum of the i^{th} species, must approximately hold for this process to occur conserving energy and momentum. Because the second inequality might not be satisfied, particularly at lower densities, [Chiu & Salpeter \(1964\)](#) proposed the so-called “modified Urca process” (mUrca)



where another nucleon N participates in the reaction absorbing momentum ([Shapiro & Teukolsky, 1983](#)). Because the equation of state we shall use (see [Sec. 2.1.1](#)) does not satisfy the condition (1.9), we will only consider the mUrca reactions as the main cooling mechanism. We recall that mUrca process provides a minimum cooling rate for a non-superfluid star.

Therefore, for mUrca reactions, the time-scale at which the magnetic field readjusts is roughly (see [Sec. 2.7](#))

$$t_{\lambda B} \sim 8 \times 10^3 \left(\frac{10^{15} \text{G}}{B} \right)^2 \left(\frac{T}{10^9 \text{K}} \right)^{-6} \left(\frac{\rho}{\rho_0} \right)^{10/3} \text{ yr}. \tag{1.11}$$

1.5 Internal temperature evolution

After the proto-NS state, thermal conduction takes place in the core. However, this lasts only $t \lesssim 10\text{--}100$ yrs, and then the core becomes isothermal because it is composed by a mixture of degenerate neutrons, electrons, protons and plausibly more exotic particles (muons, hyperons, or even deconfined quark matter) that have very high thermal conductivity ([Glen & Sutherland, 1980](#); [Yakovlev & Pethick, 2004b](#); [Pons & Viganò, 2019](#)). In the following thermal evolution, the NS core cools mainly by neutrino emission with an associated luminosity given by [Friman & Maxwell \(1979\)](#)

$$\mathcal{L}_\nu^* = 3.1 \times 10^{39} \left(\frac{T}{10^9 \text{K}} \right)^8 \left(\frac{\rho}{\rho_0} \right)^{2/3} \text{ erg s}^{-1}, \tag{1.12}$$

for mUrca reactions. Nevertheless, the cooling can be shocked by ambipolar diffusion for a sufficiently high magnetic fields (Beloborodov & Li, 2016), or by the same mUrca reactions depending on the strength of the chemical departure (see Sec.2.5.2). In this thesis, we shall explore this last possibility.

At later stages, the star cools by thermal photons emitted from the stellar surface with a luminosity given by (Reisenegger, 2009)

$$\mathcal{L}_\gamma \sim 2 \times 10^{35} \left(\frac{T}{10^9 \text{K}} \right)^{2.2} \text{ erg s}^{-1}. \quad (1.13)$$

Since the evolution of the internal temperature is governed by the radiation from the stellar surface, it is sensitive to properties of the outer parts of the star, for example Ohmic dissipation.

This thesis is organized as follows:

In Chap. 2, we study the physical model of the magnetic field and temperature evolution, focusing on the effects of β -decays and the neutrino emissivity in a hot NS core. We develop the full set of equations to be solved numerically and discuss the relevant time-scales of each physical process.

In Chap. 3, we write the equations in dimensionless units and review some numerical details. Afterwards, we propose a strategy to easily include the temperature evolution without running any further simulation, starting from the results at constant temperature given by the code of Castillo et al. (2020).

In Chap. 4, we first present the results at constant temperature. We describe the hydro-magnetic evolution in terms of the characteristic time-scales of each physical process, and study the equilibrium configurations. Then, we include the evolution of temperature and discuss its consequences, focusing on the possible magnetic feed-back on the evolution of temperature due to non-equilibrium mUrca reactions.

Finally, in Chap. 5, we summarized our results and the conclusions are outlined.

Chapter 2

Physical Model

In this chapter we develop the general physical model and the set of equations needed to evolve the magnetic field and internal temperature in a NS core. In Sec. 2.1, we describe the full set of equations to evolve the magnetic field and densities in time. The boundary conditions imposed by the solid crust are discussed in Sec. 2.2. In Sec. 2.3, the restriction to axial symmetry is imposed, where we decompose the magnetic field into two components, poloidal and toroidal, each of which is derived from a scalar potential. Hitherto, we follow the same physical model present in [Castillo et al. \(2017\)](#) and [Castillo et al. \(2020\)](#). In the following sections, we develop the equations needed to include temperature evolution in our simulations. In Sec. 2.4, the general expression for the magnetic energy dissipation is developed, where we identify the terms that heat the core. Then, the differential equation needed to evolve the internal temperature is discussed in Sec. 2.5. Later, in Sec. 2.6, we describe the different regimes under which mUrca reactions and ambipolar diffusion operate separately. Although we focus on the former, we discuss both cases for completeness. Finally, in Sec. 2.7, we describe the relevant short and long-term time-scales for each physical process.

2.1 Evolution of the magnetic field

Based on the model of Goldreich & Reisenegger (1992) and Hoyos et al. (2008), we model the interior of an isolated neutron star as npe matter, i.e., as a plasma composed of neutrons, protons, and electrons. The species are coupled by collisional and electromagnetic forces, and their equations of motions are given by

$$n_i \frac{\mu_i}{c^2} \frac{d\mathbf{v}_i}{dt} = n_i q_i \left(\mathbf{E} + \frac{\mathbf{v}_i}{c} \times \mathbf{B} \right) - n_i \nabla \mu_i - \frac{n_i \mu_i}{c^2} \nabla \Psi - \sum_{j \neq i} \gamma_{ij} n_i n_j (\mathbf{v}_i - \mathbf{v}_j), \quad (2.1)$$

where n_i and μ_i ($i = n, p, e$) are the number density and chemical potential of the i^{th} species, respectively; μ_i/c^2 is the effective mass of each particle, which could include corrections due to strong interactions and relativistic effects (Akmal et al., 1998); $q_i = \pm e$ are the electron and proton charges; and \mathbf{v}_i is the velocity of the i^{th} species. We assume charge neutrality, so at all time $n_p = n_e \equiv n_c$. The forces acting on particles are, from left to right, the Lorentz force (where \mathbf{E} and \mathbf{B} are the electric and magnetic field), the degeneracy-pressure gradient of species i , the gravitational force acting on each fluid species (where Ψ is the gravitational potential), and the frictional drag forces due to collisions between particles of different species. The later are parametrized by rate coefficients γ_{ij} , so that momentum conservation implies $\gamma_{ij} = \gamma_{ji}$.

An unbalanced magnetic force in a fluid core will induce Alfvén and sound waves, which will very quickly take the star to a magneto-hydrostatic quasi-equilibrium state in which all the forces on each fluid element are close to balancing each other. The time-scale to reach this state is a few Alfvén times $t_A \sim (10^{14} \text{ G}/B) \text{ s}$. Since we are interested in the long-term evolution of the field, which happens on much longer timescales, $\sim 10^3\text{--}10^7 \text{ yr}$, we do not intend to follow the propagation of sound waves, gravity (buoyancy) waves, and Alfvén waves in detail. Instead, we filter them out by replacing the inertial terms on the left-hand-side of the equations of motion by an artificial frictional force acting on the neutrons, of the form $\mathbf{f}_\zeta \equiv -\zeta n_n \mathbf{v}_n$ (Hoyos et al., 2008). The balance between this and the other forces acting on a fluid element determines the velocity field \mathbf{v}_n , which quickly restores the hydro-magnetic quasi-equilibrium by rearranging the particles and magnetic field on a time-scale set by the parameter ζ . The value of this parameter is chosen to be small enough so its associated time-scale is much longer than the dynamical time-scales (\sim Alfvén times), but shorter than the time-scales relevant to us.

The equations of motion then become:

$$0 = -n_n \nabla \mu_n - \frac{n_n \mu_n}{c^2} \nabla \Psi - \gamma_{ne} n_n n_c (\mathbf{v}_n - \mathbf{v}_e) - \gamma_{np} n_n n_c (\mathbf{v}_n - \mathbf{v}_p) - \zeta n_n \mathbf{v}_n, \quad (2.2)$$

$$0 = +n_c e \left(\mathbf{E} + \frac{\mathbf{v}_p}{c} \times \mathbf{B} \right) - n_c \nabla \mu_p - \frac{n_c \mu_p}{c^2} \nabla \Psi - \gamma_{pe} n_c^2 (\mathbf{v}_p - \mathbf{v}_e) - \gamma_{pn} n_c n_n (\mathbf{v}_p - \mathbf{v}_n), \quad (2.3)$$

$$0 = -n_c e \left(\mathbf{E} + \frac{\mathbf{v}_e}{c} \times \mathbf{B} \right) - n_c \nabla \mu_e - \frac{n_c \mu_e}{c^2} \nabla \Psi \quad (2.4)$$

$$- \gamma_{ep} n_c^2 (\mathbf{v}_e - \mathbf{v}_p) - \gamma_{en} n_c n_n (\mathbf{v}_e - \mathbf{v}_n).$$

Multiplying equation (2.3) with γ_{en} and (2.4) with γ_{pn} , and then subtracting them, we get the electric field

$$\mathbf{E} = - \frac{\gamma_{pn} \mathbf{v}_e + \gamma_{en} \mathbf{v}_p}{c \gamma_{cn}} \times \mathbf{B} + \frac{\mathbf{J}}{\sigma} \quad (2.5)$$

$$+ \frac{\gamma_{en} \nabla \mu_p - \gamma_{pn} \nabla \mu_e}{e \gamma_{cn}} + \frac{\gamma_{en} \mu_p - \gamma_{pn} \mu_e}{e c^2 \gamma_{cn}} \nabla \Psi,$$

where $\gamma_{cn} = \gamma_{pn} + \gamma_{en}$ is the net collisional coupling between charge particles and neutrons,

$$\sigma = e^2 \left(\gamma_{pe} + \frac{\gamma_{en} \gamma_{pn} n_n}{\gamma_{cn} n_c} \right)^{-1} \quad (2.6)$$

is the electric conductivity, and \mathbf{J} is the electric current density $\mathbf{J} = n_c e (\mathbf{v}_p - \mathbf{v}_e) = c \nabla \times \mathbf{B} / 4\pi$. We define the ‘‘ambipolar diffusion velocity’’, which represents the joint motion of the two charged particle species relative to the neutrons, as

$$\mathbf{v}_{ad} = \frac{\gamma_{pn} (\mathbf{v}_p - \mathbf{v}_n) + \gamma_{en} (\mathbf{v}_e - \mathbf{v}_n)}{\gamma_{cn}}, \quad (2.7)$$

and the ‘‘Hall drift velocity’’, which is proportional to the electric current, as

$$\mathbf{v}_H = - \frac{\gamma_{pn} - \gamma_{en}}{\gamma_{cn}} (\mathbf{v}_p - \mathbf{v}_e) = - \frac{\gamma_{pn} - \gamma_{en}}{\gamma_{cn}} \frac{\mathbf{J}}{n_c e}. \quad (2.8)$$

Hence, $(\gamma_{pn} \mathbf{v}_e + \gamma_{en} \mathbf{v}_p) / \gamma_{cn} = \mathbf{v}_n + \mathbf{v}_{ad} + \mathbf{v}_H$, so the evolution equation for the magnetic field is obtained from Faraday’s induction law as

$$\frac{\partial \mathbf{B}}{\partial t} = \nabla \times \left[(\mathbf{v}_n + \mathbf{v}_{ad} + \mathbf{v}_H) \times \mathbf{B} - \frac{c}{\sigma} \mathbf{J} \right]$$

$$- \nabla \left(\frac{c \gamma_{en}}{e \gamma_{cn}} \right) \times \nabla \mu_c - \nabla \left(\frac{\mu_p \gamma_{en} - \mu_e \gamma_{pn}}{e c \gamma_{cn}} \right) \times \nabla \Psi, \quad (2.9)$$

where we defined a total chemical potential for the charged particles, $\mu_c \equiv \mu_p + \mu_e$. The last term inside the squared brackets represents Ohmic dissipation, and the two last terms represent battery effects. As discussed in [Goldreich & Reisenegger \(1992\)](#), In the core of NSs the effects of Hall drift and Ohmic decay can be orders of magnitude smaller than the ambipolar diffusion, hence we neglect those terms. Also, [Castillo et al. \(2017\)](#) showed that the time-scale on which the battery terms are relevant is roughly the same as the Hall time-scale, therefore we also neglect those terms, obtaining

$$\frac{\partial \mathbf{B}}{\partial t} = \nabla \times (\mathbf{v}_c \times \mathbf{B}), \quad (2.10)$$

where $\mathbf{v}_c \equiv \mathbf{v}_{ad} + \mathbf{v}_n$ is the charged particle velocity. By adding equations (2.2), (2.3), and (2.4), we get the velocity field of the neutrons, parametrized by the fictitious friction coefficient ζ , which replaces the very small inertial terms,

$$\mathbf{v}_n = \frac{1}{\zeta n_n} \left[\frac{\mathbf{J}}{c} \times \mathbf{B} - n_c \left(\nabla \mu_c + \frac{\mu_c}{c^2} \nabla \Psi \right) - n_n \left(\nabla \mu_n + \frac{\mu_n}{c^2} \nabla \Psi \right) \right]. \quad (2.11)$$

From equations (2.3), (2.4), and (2.7) we obtain the ambipolar diffusion velocity

$$\mathbf{v}_{ad} = \frac{1}{\gamma_{cn} n_c n_n} \left[\frac{\mathbf{J}}{c} \times \mathbf{B} - n_c \left(\nabla \mu_c + \frac{\mu_c}{c^2} \nabla \Psi \right) \right], \quad (2.12)$$

which is proportional to the imbalance between the forces, including (from left to right) the magnetic force density, the gradient of the degeneracy pressure of the charged particles, and the gravitational force on the charged particles. Thus, the ambipolar diffusion is driven by the magnetic force, controlled by the pressure gradient and gravitational forces acting on the charged particles, and opposed by the collisional drag of the neutrons. The terms in equation (2.11) for the neutron velocity have an analogous interpretation.

To evolve the particle densities, we use the continuity equations

$$\frac{\partial n_c}{\partial t} + \nabla \cdot (n_c \mathbf{v}_c) = +\Delta \Gamma, \quad (2.13)$$

$$\frac{\partial n_n}{\partial t} + \nabla \cdot (n_n \mathbf{v}_n) = -\Delta \Gamma, \quad (2.14)$$

where $\Delta \Gamma$ is the net conversion rate of charged particles to neutrons by weak interactions, i.e., the difference between the rates for the (direct or modified) Urca processes, $\Delta \Gamma \equiv \Gamma(p + e \rightarrow n + \nu_e) - \Gamma(n \rightarrow p + e + \bar{\nu}_e)$. The analytical form of this quantity shall be discussed in more details in Sec. 2.5.2.

2.1.1 Background NS model

Since the ratio between the magnetic and degeneracy pressure P in the interior of NSs is $B^2/8\pi P \leq 10^{-6}$, we consider that the magnetic field induces only small perturbations with respect to a hypothetical non-magnetized stellar structure (e. g., [Reisenegger 2009](#)). Thus, we split the particle densities, and hence the chemical potentials, in two:

1. time-independent background densities $n_i(r)$ and chemical potentials $\mu_i(r)$ determined by the conditions of chemical β -equilibrium,

$$\mu_n = \mu_c = \mu(r), \quad (2.15)$$

and hydrostatic equilibrium in the absence of the magnetic field,

$$\nabla \mu + \frac{\mu}{c^2} \nabla \Psi = 0, \quad (2.16)$$

and

2. much smaller time-dependent perturbations δn_c , δn_n , and $\delta\mu_c$, $\delta\mu_n$, induced by the evolving magnetic field (to be discussed in Sec. 2.1.2).

As in [Castillo et al. \(2020\)](#), we consider the non-magnetized background star to have non-uniform particle densities, with different radial gradients for the neutrons and charged particles, as imposed by β -equilibrium. For simplicity, we consider a toy model equation of state, in which we ignore strong interactions, treating neutrons and protons (with the same mass m) as non-relativistic Fermi gases, and electrons as an extremely relativistic (massless) Fermi gas. Thus, the chemical potentials are related to the particle densities by

$$\mu_n(r) = mc^2 + \frac{p_{Fn}(r)^2}{2m}, \quad (2.17)$$

$$\mu_c(r) = mc^2 + \frac{p_{Fc}(r)^2}{2m} + p_{Fc}(r)c, \quad (2.18)$$

where $p_{Fi} = \hbar [3\pi^2 n_i(r)]^{1/3}$ are the Fermi momenta of neutrons ($i = n$) and charged particles ($i = c$). Since we assume charge neutrality, the densities (and thus the Fermi momenta) of protons and electrons are the same. Thus, the condition of chemical equilibrium (equation [2.15]) allows to write the density of neutrons in terms of that of the charged particles,

$$n_n(r) = \left[\frac{2mc}{\hbar(3\pi^2)^{1/3}} n_c(r)^{1/3} + n_c(r)^{2/3} \right]^{3/2}. \quad (2.19)$$

For the background number density of charged particles, we used the simple analytical relation

$$n_c(r) = n_{c0} \left[\frac{\sin(0.7\pi r/R)}{0.7\pi r/R} \right]^6 \quad (2.20)$$

which closely resembles the numerical solution obtained by imposing Newtonian hydrostatic equilibrium (equation [2.16]) on this Fermi gas, and we adjusted the central density so $\varepsilon = n_n(0)/n_c(0) \approx 10$, yielding a star of mass $1.58 M_\odot$, and radius 8.2 km. The transport coefficients $\gamma_{ij}(r, T)$ between species i and j are computed from the relations derived for the collision times $\tau_{ij}(r, T)$ by [Yakovlev & Shalybkov \(1990\)](#), where T denotes the core temperature. This stellar model, although very simplified, allows us to capture the effects of radial density gradients, gravity, and stable stratification into our simulations.

2.1.2 Linearization

As the perturbations to the particle density profiles are small (similarly small as $B^2/8\pi P \leq 10^{-6}$), we can apply Eulerian perturbation to linearize, namely,

$$\delta\mu_i = K_{ii}\delta n_i; \quad K_{ii} = \frac{\partial\mu_i}{\partial n_i}, \quad (2.21)$$

where $i = n, c$. For a realistic equation of state, the off-diagonal terms $K_{ij} = K_{ji} = \partial\mu_i/\partial n_j$, must be considered because protons and neutrons interact via strong interaction. Hence, the small perturbations $\delta\mu_n$ and $\delta\mu_c$ would also depend on δn_c and δn_n , respectively. However, and for simplicity, in this work we restricted to the equation of state just discussed in Sec. 2.1.1. Finally, dropping higher-order terms, we can write the full set of linearized equations,

$$\frac{\partial \mathbf{B}}{\partial t} = \nabla \times (\mathbf{v}_c \times \mathbf{B}), \quad (2.22)$$

$$\frac{\partial \delta n_n}{\partial t} + \nabla \cdot (n_n \mathbf{v}_n) = +\Delta \Gamma, \quad (2.23)$$

$$\frac{\partial \delta n_c}{\partial t} + \nabla \cdot (n_c \mathbf{v}_c) = -\Delta \Gamma, \quad (2.24)$$

$$\mathbf{v}_n = \frac{1}{\zeta n_n} (\mathbf{f}_B + \mathbf{f}_n + \mathbf{f}_c), \quad (2.25)$$

$$\mathbf{v}_{ad} = \frac{1}{\gamma_{cn} n_c n_n} (\mathbf{f}_B + \mathbf{f}_c), \quad (2.26)$$

$$\mathbf{f}_B = \frac{(\nabla \times \mathbf{B}) \times \mathbf{B}}{4\pi}, \quad (2.27)$$

$$\mathbf{f}_n = -n_n \mu \nabla \left(\frac{\delta \mu_n}{\mu} \right), \quad (2.28)$$

$$\mathbf{f}_c = -n_c \mu \nabla \left(\frac{\delta \mu_c}{\mu} \right), \quad (2.29)$$

$$\mathbf{v}_c = \mathbf{v}_n + \mathbf{v}_{ad}, \quad (2.30)$$

$$\delta \mu_c = K_{cc} \delta n_c, \quad (2.31)$$

$$\delta \mu_n = K_{nn} \delta n_n. \quad (2.32)$$

2.2 Boundary conditions

We assume the currents in the crust decay much faster than typical evolution time-scales in the core, so we can treat the crust as a vacuum whose magnetic field at any time is fully determined by the field in the core (see [Castillo et al. 2017](#) for more details on the imposed boundary conditions). This external current-free magnetic field is computed at all time-steps as a multipolar expansion, whose coefficients (a_ℓ , with $\ell = 1, 2, \dots$) are determined by the value of the radial component of the magnetic field at the crust-core interface. These coefficients also determine the energy stored in the external magnetic field, namely

$$E_B^{\text{ext}} = \sum_{\ell=1}^{\infty} E_{B,\ell}^{\text{ext}} = \sum_{\ell=1}^{\infty} \frac{\ell+1}{2\ell+1} \frac{a_\ell^2}{2}, \quad (2.33)$$

where $E_{B,\ell}^{\text{ext}}$ is the energy stored in the ℓ -th component of the external field. Further details on the external field and boundary conditions can be seen in [Castillo et al. \(2017\)](#). Also, at the crust-core interface we assume that the radial components of both the neutron velocity \mathbf{v}_n and the charged-particle velocity \mathbf{v}_c are null. Therefore, at the crust-core interface we have

$$\frac{\partial}{\partial r} \begin{pmatrix} \delta\mu_c \\ \mu \end{pmatrix} = \frac{f_B^r}{n_c \mu} \quad (2.34)$$

$$\frac{\partial}{\partial r} \begin{pmatrix} \delta\mu_n \\ \mu \end{pmatrix} = 0 \quad (2.35)$$

2.3 Axially symmetric fields

We restrict ourselves to axial symmetry, so the magnetic field can be decomposed as (see [Castillo et al. 2020](#)),

$$\mathbf{B} = \nabla\alpha \times \nabla\phi + \beta\nabla\phi, \quad (2.36)$$

where the scalar potentials $\alpha(t, r, \theta)$ and $\beta(t, r, \theta)$ generate the poloidal and toroidal magnetic field, respectively. Here, t denotes time, r is the radial coordinate, and θ and ϕ are the polar and azimuthal angles, respectively; so $\nabla\phi = \hat{\phi}/(r \sin\theta)$. An explicit form for the evolution of the magnetic potentials can be derived from equation (2.22), where we get

$$\frac{\partial\alpha}{\partial t} = -\mathbf{v}_c \cdot \nabla\alpha, \quad (2.37)$$

$$\frac{\partial\beta}{\partial t} = r^2 \sin^2\theta \nabla \cdot \left[\frac{(\mathbf{v}_c \times \mathbf{B}) \times \hat{\phi}}{r \sin\theta} \right] \quad (2.38)$$

2.4 Energy Dissipation

The magnetic field affects the internal energy of the background star by dissipating part of the magnetic energy in the NS core, and by enhancing the

internal energy of the fluid. In this section, we study the different contributions (magnetic and particles) to the energy and its time derivative, focusing on the terms that heat the core:

2.4.1 Energy stored in the density perturbations

The variation of energy stored in the particles of i^{th} species (i.e. in the Fermi sea, $i = p, n, e$) $\delta E_{F,i}$ induced by the magnetic field, can be written as (see [Castillo et al. 2017](#))

$$\delta E_{F,i} = \int_V \left(\mu \delta n_i + \frac{\delta n_i \delta \mu_i}{2} \right) d^3x. \quad (2.39)$$

Analogously, it can be shown that the variation of gravitational energy also induced by the magnetic field, reads as

$$\delta E_{\Psi,i} = \int_V \left(\mu \delta n_i + \frac{\delta n_i \delta \mu_i}{2} \right) \frac{\Psi}{c^2} d^3x. \quad (2.40)$$

Adding equations (2.39) and (2.40) for both neutrons and charged particles, the time rate of energy stored (internal and gravitational), is given by

$$\delta \dot{E}_{Ig} = \int_V \left(\frac{\partial \delta n_c}{\partial t} \delta \mu_c^\infty + \frac{\partial \delta n_n}{\partial t} \delta \mu_n^\infty \right) d^3x, \quad (2.41)$$

where $\delta \mu_i^\infty = \delta \mu_i e^{\psi/c^2}$ ($i = c, n$) are the redshifted chemical deviations which, up to first order, give the original expression for a Newtonian star ($\Psi/c^2 \ll 1$), $\delta \mu_i^\infty \simeq \delta \mu_i$. Here in equation (2.41), we neglected the term

$$\int_V \mu (\delta n_c + \delta n_n) \left(1 + \frac{\psi}{c^2} \right) d^3x \simeq \int_V \mu^\infty (\delta n_c + \delta n_n) d^3x, \quad (2.42)$$

because the redshifted chemical potential of the background, μ^∞ , is uniform as a consequence of the hydrostatical equilibrium condition equation (2.16),

$$\nabla \mu^\infty = (\nabla \mu + (\mu/c^2) \nabla \Psi) e^{\Psi/c^2} = 0, \quad (2.43)$$

and the perturbations preserve the baryon number through the core's volume, i.e., $\int_V (\delta n_c + \delta n_n) d^3x = 0$.

2.4.2 Energy stored by the magnetic field

Starting from the Poynting theorem, the variation of the magnetic energy per unit time is given by

$$\dot{E}_B = - \int_V \mathbf{J} \cdot \mathbf{E} d^3x - \frac{1}{4\pi} \oint_{\partial V} \mathbf{B} \times (\mathbf{v}_c \times \mathbf{B}) \cdot d\mathbf{S}, \quad (2.44)$$

where $d\mathbf{S}$ is a surface element outward normal to the surface ∂V defined by the crust-core interface. We identify the second term on the right-hand side (without

the minus sign) as dE_B^{ext}/dt , corresponding to the Poynting flux through the surface $d\mathbf{S}$, which we here and hereafter denote as \mathcal{L}_P .

With the aid of equation (2.5), the Joule term can be written as

$$-\int_V \mathbf{J} \cdot \mathbf{E} d^3x = \int_V \frac{\mathbf{J}}{c} \cdot (\mathbf{v}_c \times \mathbf{B}) = -\int_V (\mathbf{v}_n + \mathbf{v}_{ad}) \cdot \frac{\mathbf{J} \times \mathbf{B}}{c}, \quad (2.45)$$

where the Hall, Ohm and battery terms were neglected (Goldreich & Reisenegger, 1992). From equation (2.11), $(\mathbf{J} \times \mathbf{B})/c$ can be replaced by

$$\begin{aligned} -\int_V \mathbf{J} \cdot \mathbf{E} d^3x &= -\int_V \zeta n_n \mathbf{v}_n \cdot (\mathbf{v}_n + \mathbf{v}_{ad}) d^3x \\ &\quad -\int_V n_c (\mathbf{v}_n + \mathbf{v}_{ad}) \cdot \nabla \delta\mu_c^\infty d^3x \\ &\quad -\int_V n_n (\mathbf{v}_n + \mathbf{v}_{ad}) \cdot \nabla \delta\mu_n^\infty d^3x, \end{aligned} \quad (2.46)$$

where we wrote again the pressure and the gravity forces in terms of the redshifted deviations. One further step is to write the neutron velocity in terms of the ambipolar one, $\mathbf{v}_n = (1/\zeta n_n)(\gamma_{cn} n_c n_n \mathbf{v}_{ad} - n_n \nabla \delta\mu_n^\infty)$, then integrating by parts using the continuity equations (2.23) and (2.24) (the boundary terms can be neglected because we set $v_{ad,r} = v_{n,r} = 0$, as discussed in Sec. 2.2, to finally obtain

$$\begin{aligned} -\int_V \mathbf{J} \cdot \mathbf{E} d^3x &= -\int_V \zeta n_n |\mathbf{v}_n|^2 d^3x - \int_V \gamma_{cn} n_c n_n |\mathbf{v}_{ad}|^2 d^3x \\ &\quad - \int_V \Delta\Gamma \Delta\mu^\infty d^3x - \int_V \left(\frac{\partial \delta n_c}{\partial t} \delta\mu_c^\infty + \frac{\partial \delta n_n}{\partial t} \delta\mu_n^\infty \right) d^3x, \end{aligned} \quad (2.47)$$

where $\Delta\mu^\infty \equiv \delta\mu_n^\infty - \delta\mu_c^\infty$ is the redshifted chemical imbalance. Therefore, the rate of change of the magnetic energy stored in the core reads as

$$\dot{E}_B = -\mathcal{L}_\zeta - \mathcal{L}_{ad} - \mathcal{L}_{H\nu} - \delta\dot{E}_{Ig} - \mathcal{L}_P, \quad (2.48)$$

where \mathcal{L}_{ad} and $\mathcal{L}_{H\nu}$ are the ambipolar and chemical energy released inside the core and \mathcal{L}_ζ is the power released due to the artificial friction. Each term reads as

$$\mathcal{L}_{H\nu} = \int_V \Delta\Gamma \Delta\mu d^3x, \quad (2.49)$$

$$\mathcal{L}_{ad} = \int_V \gamma_{cn} n_c n_n |\mathbf{v}_{ad}|^2 d^3x, \quad (2.50)$$

$$\mathcal{L}_\zeta = \int_V \zeta n_n |\mathbf{v}_n|^2 d^3x, \quad (2.51)$$

here the simplification $\Delta\mu^\infty \simeq \Delta\mu$ has been taken (see, e.g., Gusakov et al. 2017, for details and references).

2.5 Temperature evolution

After the thermal relaxation stage, heat conduction in the NS core proceeds almost instantaneously and an isothermal interior is a good approximation. Thus, the evolution of the internal temperature is given by a thermal balance equation (see [Thorne 1977](#) for its general relativistic version)

$$\frac{dT}{dt} = \frac{1}{C} (\mathcal{L}_H - \mathcal{L}_\nu), \quad (2.52)$$

where C is the total heat capacity of the star (for more details about its possible values see [Cumming et al. 2017](#)), \mathcal{L}_H is the total power released by the possible heating mechanisms, and \mathcal{L}_ν is the total neutrino luminosity.

2.5.1 Heat capacity

The heat capacity in equation (2.52) for degenerate, non-superfluid fermions (see, e. g., [Levenfish & Yakovlev 1994](#), and [Cumming et al. 2017](#)) is given by

$$C = \frac{k_B^2 T}{3\hbar^3} \sum_{i=n,p,e} \int_V m_i^*(n_b) p_{Fi}(n_b) d^3x, \quad (2.53)$$

where p_{Fi} , n_b , and m_i^* are the Fermi momentum, baryon number density and effective mass of the i^{th} species, respectively. The value of C , for the equation of state we are using, is approximately

$$C \approx 3 \times 10^{39} \left(\frac{T}{10^9 \text{ K}} \right) \text{ erg K}^{-1}. \quad (2.54)$$

2.5.2 Neutrino luminosity

If the magnetic field were not present, the NS core would remain as barotropic matter in chemical equilibrium and passively cooling with the equilibrium luminosity due to mUrca reactions given by [Friman & Maxwell \(1979\)](#)

$$\mathcal{L}_\nu^* = 3.1 \times 10^{39} \left(\frac{T}{10^9 \text{ K}} \right)^8 \left(\frac{\rho}{\rho_0} \right)^{2/3} \text{ erg s}^{-1}, \quad (2.55)$$

where $\rho_0 = 2.8 \times 10^{14} \text{ g cm}^{-3}$ is the nuclear saturation density. However, the magnetic field induces small local departures from chemical equilibrium, altering the net neutrino luminosity. The analytical expressions for the neutrino luminosity \mathcal{L}_ν and the net emission rate $\Delta\Gamma$, away from equilibrium and for non-superfluid matter were found by [Haensel \(1992\)](#), namely,

$$\mathcal{L}_\nu = \int_V \epsilon_\nu^*(n_b, T) F(\xi) d^3x, \quad (2.56)$$

$$\Delta\Gamma(n_b, \xi) = \frac{\epsilon_\nu^*(n_b, T)}{k_B T} H(\xi), \quad (2.57)$$

where ϵ_ν^* is the equilibrium neutrino emissivity, which is only a function of temperature T and the baryon number density n_b , and $F(\xi)$ and $H(\xi)$ are dimensionless control functions of $\xi = \Delta\mu/k_B T$ (a variable that quantifies the departure from equilibrium). The exact expressions of $H(\xi)$ and $F(\xi)$ were found by [Reisenegger \(1995\)](#) as

$$F(\xi) = 1 + \frac{22020\xi^2}{11513\pi^2} + \frac{5670\xi^4}{11513\pi^4} + \frac{420\xi^6}{11513\pi^6} + \frac{9\xi^8}{11513\pi^8}, \quad (2.58)$$

$$H(\xi) = \frac{14680\xi}{11513\pi^2} + \frac{7560\xi^3}{11513\pi^4} + \frac{840\xi^5}{11513\pi^6} + \frac{24\xi^7}{11513\pi^8}. \quad (2.59)$$

The main effect of non-equilibrium mUrca reactions is a local amount of energy released per reaction, $\Delta\mu\Delta\Gamma$, that heats the core and enhances the neutrino luminosity, quantified by $F(\xi)$ in equation (2.56). This point can be specified in terms of ξ by taking the difference of the heating term (neutrino power released) and the luminosity, equation (2.49) and (2.56), which with aid of equation (2.58), and (2.59) reads as

$$\mathcal{L}_{H\nu} - \mathcal{L}_\nu = \int_V \epsilon_\nu^*(n_b, T) M(\xi) d^3x, \quad (2.60)$$

where we have introduced a new function

$$M(\xi) = \frac{\Delta\Gamma\Delta\mu - \epsilon_\nu}{\epsilon_\nu^*} = \xi H(\xi) - F(\xi). \quad (2.61)$$

For small $|\xi|$, we may approximate this function by

$$M_{app}(\xi) \simeq -\frac{7340\xi^2}{11513\pi^2} - 1, \quad (2.62)$$

which is found by taking the functions $F(\xi)$ and $\xi H(\xi)$ up to quadratic order,

$$H(\xi) \simeq \frac{14680\xi}{11513\pi^2}, \quad (2.63)$$

$$F(\xi) \simeq 1 + \frac{22020\xi^2}{11513\pi^2}. \quad (2.64)$$

Fig. 2.1 shows the behavior of $M(\xi)$, and the approximation to this function $M_{app}(\xi)$. When the departure from equilibrium is modest, namely $|\xi| \lesssim 3$, the function $M_{app}(\xi)$ is a good approximation and mUrca reactions release more thermal energy from the core due to a stronger neutrino emission. This is known as the ‘‘subthermal’’ regime or approximation ([Haensel et al., 2002](#)), and is also characterized by a net emission rate proportional to the chemical imbalance

$$\Delta\Gamma = \lambda\Delta\mu, \quad (2.65)$$

where λ is the net emission rate per unit energy and reads as

$$\begin{aligned} \lambda &= \frac{14680}{11513\pi^2(k_B T)^2} \epsilon_\nu^*(n_b, T) \\ &\simeq 5 \times 10^{33} \left(\frac{T}{10^9 \text{ K}} \right)^6 \left(\frac{\rho}{\rho_0} \right)^{2/3} \text{ erg}^{-1} \text{ cm}^{-3} \text{ s}^{-1} \end{aligned} \quad (2.66)$$

On the other hand, Fig. 2.1 shows that when departures from chemical equilibrium are $\xi \gtrsim 5$, mUrca reactions leave more thermal energy inside the core, and a net heating can occur. This regime is called “suprathermal”.

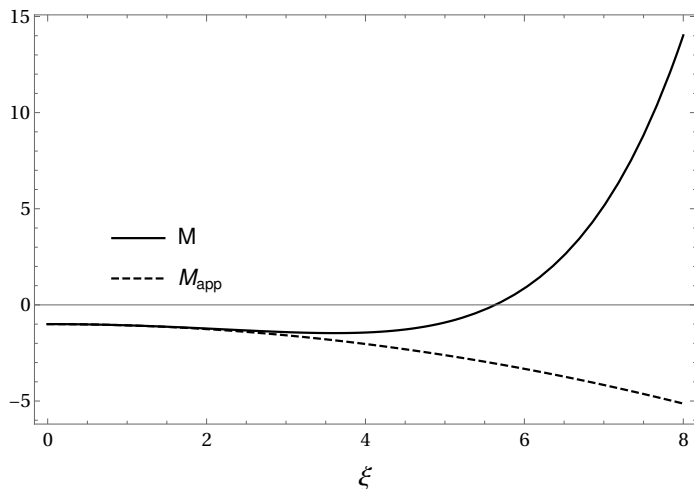


Figure 2.1: Function $M_M(\xi)$ and its approximation $M_{app}(\xi)$ in the sub-thermal case given by equations (2.63) and (2.64).

In equation (2.48), the terms \mathcal{L}_P and δE_{Ig} do not contribute to the entropy generation in the core. In fact, the Poynting flux may inject magnetic energy from outside into the core (see Chap. 4) and δE_{Ig} is conversion from magnetic to internal energy. Only terms the \mathcal{L}_ζ , \mathcal{L}_{ad} , and $\mathcal{L}_{H\nu}$ dissipate magnetic energy (see Gusakov et al. 2017 for a more detailed discussion). Therefore, using equations (2.49)-(2.51), (2.52), and (2.61), the most general equation for the temperature rate is

$$\frac{dT}{dt} = \frac{1}{C} (\mathcal{L}_\zeta + \mathcal{L}_{ad} - \mathcal{L}_\nu^{\text{eff}}), \quad (2.67)$$

where $\mathcal{L}_\nu^{\text{eff}} \equiv \mathcal{L}_\nu - \mathcal{L}_{H\nu}$ is the effective neutrino luminosity.

2.6 Strong and weak-coupling regimes

The underlying physics associated to the magnetic field decay has two different regimes depending on the internal temperature of the NS. At the early epoch of the star’s life, the magnetic evolution in the core is dominated by the mUrca reactions and for later times by ambipolar diffusion. To quantify this, let us estimate the quotient between the neutrino chemical and the ambipolar power released, which, for the simple equation of state we use, gives roughly

$$\frac{\mathcal{L}_{H\nu}}{\mathcal{L}_{ad}} \sim \frac{\lambda \Delta \mu^2}{\gamma_{cn} n_n n_c v_{ad}^2} \sim \left(\frac{T}{T_{eq}} \right)^8, \quad (2.68)$$

where

$$T_{eq} \sim 5 \times 10^8 \left(\frac{L}{1\text{km}} \right)^{-1/4} \text{ K} \quad (2.69)$$

is the temperature at which ambipolar diffusion and non-equilibrium mUrca reactions contribute equally to the dissipation of magnetic energy in the core. Here, L is the typical length scale of the magnetic field.

In the case of passive cooling, the internal temperature and time are related by $t \approx (T/10^9 \text{ K})^{-6} \text{ yr}$ (Beloborodov & Li, 2016). So the core cools to 10^9 K in about 1 year. Thus, T_{eq} should be reached very early in the thermal history of the star, at $t_{eq} \approx 64 \text{ yr}$.

In the previous estimation, we used the “subthermal” regime because, for a hot NS, it is a good first approximation. Indeed, the order of magnitude of $|\xi|$ is (Reisenegger, 2009)

$$\frac{|\Delta\mu|}{k_B T} \sim 3 \left(\frac{B}{10^{16} \text{ G}} \right)^2 \left(\frac{T}{10^9 \text{ K}} \right)^{-1}. \quad (2.70)$$

Therefore, using the result in equation (2.68), we may distinguish the two regimes:

2.6.1 Strong Coupling

At high temperatures $T > T_{eq}$, charged particles and neutrons are strongly coupled by collisions, and can convert into each other by mUrca reactions. Thus, the core matter can be considered as a single fluid that gradually changes its composition as it moves radially with a speed proportional to the mUrca reaction rate, but much slower than the neutrino cooling time (Reisenegger, 2009; Ofengeim & Gusakov, 2018). Therefore, this regime is described by setting the ambipolar velocity to zero in the set of equations (2.22)-(2.32), thus $\mathbf{v}_n = \mathbf{v}_c \equiv \mathbf{v}$;

$$\frac{\partial \mathbf{B}}{\partial t} = \nabla \times (\mathbf{v} \times \mathbf{B}), \quad (2.71)$$

$$\frac{\partial \delta n_n}{\partial t} + \nabla \cdot (n_n \mathbf{v}) = +\lambda \Delta \mu, \quad (2.72)$$

$$\frac{\partial \delta n_c}{\partial t} + \nabla \cdot (n_c \mathbf{v}) = -\lambda \Delta \mu, \quad (2.73)$$

$$\mathbf{v} = \frac{1}{\zeta n_n} (\mathbf{f}_B + \mathbf{f}_n + \mathbf{f}_c), \quad (2.74)$$

$$\frac{dT}{dt} = \frac{1}{C} \left(\mathcal{L}_\zeta - \frac{\mathcal{L}_{H\nu}}{2} - \mathcal{L}_\nu^* \right), \quad (2.75)$$

$$(2.76)$$

$$\Delta \mu = \delta \mu_c - \delta \mu_n. \quad (2.77)$$

where we used $\mathcal{L}_\nu^{\text{eff}}(\xi \lesssim 3) \approx \mathcal{L}_{\text{H}\nu}/2 + \mathcal{L}_\nu^{*1}$, which was obtained by replacing equation (2.62) into equation (2.60).

2.6.2 Weak Coupling

At low temperatures $T < T_{eq}$, mUrca reactions are essentially frozen, but the collision rate between neutrons and charged particles is also strongly suppressed, therefore it becomes possible for these two components to move separately, with different velocity fields, in this way allowing the composition to adjust to its equilibrium state at any given density. Thus, setting the right hand side of equations (2.23) and (2.24) to zero, allows us to describe this regime. As we have said, this regime has been studied in details by [Castillo et al. \(2017\)](#) and [Castillo et al. \(2020\)](#).

2.7 Time-scales

As we just discussed in Sec. 2.1, solving the entire dynamics, including inertial terms, implies following the relaxation due to sound, gravity and Alfvén waves, which happens much faster than the time-scales of interest. This short dynamics was mimicked by [Castillo et al. \(2020\)](#) in the weak coupling regime: Starting with arbitrary initial conditions, the parameter ζ was chosen so that \mathbf{f}_ζ reduced the net force imbalance on a fluid element (in round brackets on the right-hand side of equation [2.25]) by bulk motions (with velocity \mathbf{v}_n), reaching the hydro-magnetic quasi-equilibrium much more quickly than the force imbalance on the charged-particle component (in round brackets on the right-hand side of equation [2.26]) is reduced by ambipolar diffusion (with relative velocity \mathbf{v}_{ad}). For the strong coupling regime, however, there is a single velocity field ($\mathbf{v} \equiv \mathbf{v}_n = \mathbf{v}_{ad}$) that first leads to the hydro-magnetic quasi-equilibrium, and then causes the long-term evolution. In this case, the value of ζ must satisfy

$$\zeta \ll \frac{n_c^2}{\lambda n_n L_c^2}, \quad (2.78)$$

where L_c is the typical length-scale of the charged-particle flux. This condition comes from requiring that more energy is released by neutrinos than by artificial friction, i.e. $\mathcal{L}_\zeta \ll \mathcal{L}_{\text{H}\nu}$, at the time-scales of interest, when the fluid velocity is controlled by the particle conversion rate: $v \sim \lambda \Delta \mu L_c / n_c$ (see Sec. 2.7.2 for more details). In the following subsections, we shall describe the short-term evolution generated by the force \mathbf{f}_ζ , and the long-term evolution due to mUrca reactions.

¹We remark that in this case $\mathcal{L}_{\text{H}\nu}$ has a minus sign inside equation (2.75), which means a stronger cooling.

2.7.1 Short-term relaxation through fictitious friction

For the characteristic spatial scale $L \lesssim R$ of the magnetic field, the time-scale to see significant changes in the magnetic field is roughly $\sim L/v$, much larger than for the density perturbations to evolve, which are roughly $\sim (\delta n_n/n_n)(L/v)$ (from equation [2.23]) and $\sim (\delta n_c/n_c)(L/v)$ (from equation [2.24]), if $\Delta\mu = 0$ initially. Thus, for $t \ll L/v$, the magnetic field can be taken as fixed during these short scales, and only the density perturbations evolve.

Before proceeding with the analysis, we remind that for an axially symmetric magnetic field configuration, the Lorentz force (equation [2.36]) can be decomposed as

$$\mathbf{f}_B = \mathbf{f}_B^{\text{Pol}} + \mathbf{f}_B^{\text{Tor}}, \quad (2.79)$$

where $\mathbf{f}_B^{\text{Pol}}$ and $\mathbf{f}_B^{\text{Tor}}$ are the poloidal and toroidal components, respectively. On the other hand, the fluid forces given by equations (2.74) are purely poloidal, therefore they cannot balance $\mathbf{f}_B^{\text{Tor}}$. Furthermore, each of the fluid forces is proportional to the gradient of a single scalar function, therefore an arbitrary $\mathbf{f}_B^{\text{Pol}}$ can only be balanced for a particular, non-trivial combination of chemical potential perturbations, $\delta\mu_n(r, \theta)$ and $\delta\mu_c(r, \theta)$.

We choose arbitrary non-equilibrium initial conditions with no density perturbations $\delta n_n(t=0) = \delta n_c(t=0) = 0$, so initially the star is in chemical equilibrium, $\Delta\mu(t=0) = 0$. Thus, the initial bulk velocity will be $\mathbf{v}^{\text{Pol}} = \mathbf{f}_B^{\text{Pol}}/\zeta n_n$, and the density perturbations and chemical imbalance will grow roughly as $|\delta n_c/n_c| \sim |\delta n_n/n_n| \sim vt/L$, and $\Delta\mu \sim (n_c K_{cc} - K_{nn} n_n)vt/L$, respectively. This causes a growth of the fluid forces, $f_n \sim n_n^2 K_{nn} v^{\text{Pol}} t/L^2$ and $f_c \sim n_c^2 K_{cc} v^{\text{Pol}} t/L^2$, until the larger of these, namely f_n (since $K_{nn} n_n \sim K_{cc} n_c$, whereas $n_c \ll n_n$) will approach the magnitude of $\mathbf{f}_B^{\text{Pol}}$ on a time-scale

$$t_{\zeta P} \sim \frac{\zeta L^2}{K_{nn} n_n}, \quad (2.80)$$

the analog of the propagation time of sound waves when inertial effects are taken into account. However, as discussed in the previous paragraph, \mathbf{f}_n alone cannot balance an arbitrary (poloidal) vector field $\mathbf{f}_B^{\text{Pol}}(r, \theta)$. Thus, \mathbf{v} might now be a very different vector field than $\mathbf{f}_B/(\zeta n_n)$, but it will still be roughly of the same order of magnitude, further modifying the density perturbations until $\mathbf{f}_B^{\text{Pol}} + \mathbf{f}_n + \mathbf{f}_c \approx 0$, at which point the density perturbations reach the fractional magnitudes $|\delta n_i|/n_i \sim B^2/(4\pi K_{ii} n_i^2)$ ($i = c, n$) and the chemical imbalance reaches a maximum value $\Delta\mu \sim B^2/4\pi n_c$. The latter happens on a time-scale

$$t_{\zeta g} \sim \frac{L}{v} \frac{|\delta n_c|}{n_c} \sim \frac{\zeta n_n L^2}{n_c^2 K_{cc}}, \quad (2.81)$$

which should be roughly identified with the buoyancy time-scale (Brunt-Väisälä period) in a realistic NS (Reisenegger, 2009), since balancing an arbitrary $\mathbf{f}_B^{\text{Pol}}$ will generally require non-parallel vector fields $\nabla[\delta\mu_n(r, \theta, t)/\mu(r)]$ and $\nabla[\delta\mu_c(r, \theta, t)/\mu(r)]$, i.e., a baroclinic (non-barotropic) configuration.

On the other hand, this process left $\mathbf{f}_B^{\text{Tor}}$ unbalanced and it must decay to zero by rearrangement of the magnetic field, which occurs on a longer time-scale

$$t_{\zeta B} \sim \frac{L}{v} \sim \frac{4\pi n_n L^2 \zeta}{B^2}, \quad (2.82)$$

which could be identified with an Alfvén-like time. This stage, at which poloidal forces are approximately balanced and the magnetic field has already readjusted, is the so-called “hydromagnetic quasi-equilibrium”. The latter evolution also modifies $\mathbf{f}_B^{\text{Pol}}$, nevertheless, fluid displacements can keep up, always maintaining the balance between $\mathbf{f}_B^{\text{Pol}}$ and the gradient forces.

Part of these arguments are still valid when there is not axial symmetry, since two gradient forces can only balance two different components of the magnetic force (in a time-scale $t_{\zeta g}$), one component will always remain unbalanced. Therefore, reaching a state of hydromagnetic quasi-equilibrium will always require the magnetic field to adjust so that the latter component vanishes, which will happen on a time-scale $\sim t_{\zeta B}$.

2.7.2 Long-term evolution through mUrca reactions

As we have discussed in the previous section, the short-term dynamics mimicked by the fictitious friction leaves the star out of chemical equilibrium. The excess of chemical energy can only be dissipated by mUrca reactions, which in turn locally change the degeneracy pressure forces, so the magnetic field must rearrange, moving particles in such a way that a new hydrostatic equilibrium is reached.

By studying the time derivative of $\Delta\mu$, the long-term time-scales of the magneto-chemical evolution can be derived. Using equations of continuity (2.72) and (2.73), and equations (2.31) and (2.32), one gets

$$\frac{\partial}{\partial t} \Delta\mu = -\lambda(K_{cc} + K_{nn})\Delta\mu + K_{nn} \nabla \cdot (n_n \mathbf{v}) - K_{cc} \nabla \cdot (n_c \mathbf{v}). \quad (2.83)$$

Therefore, if the magnetic field were not present, $\Delta\mu$ would decrease exponentially by the effect of mUrca reactions, reaching chemical equilibrium on a time-scale given roughly by

$$t_\lambda \sim \frac{1}{\lambda(K_{cc} + K_{nn})}. \quad (2.84)$$

Although this is not the case, one can identify this time-scale as a cooling time-scale when the temperature evolution is considered because it is only ~ 10 times smaller than the passive cooling time-scale $t_c = E_T/2\dot{E}_T$ (Reisenegger, 1995) (E_T is the thermal energy).

When the magnetic field is present, it induces fluid motions that keep the force balance and compensate the effect of mUrca reactions. This can be seen in the second and third term in equation (2.83) which slow down the approach to chemical equilibrium. The time-scale of this process can be estimated by

considering that the continuity equations at this stage are expected to be

$$\nabla \cdot (n_n \mathbf{v}) \simeq \lambda \Delta \mu, \quad (2.85)$$

$$\nabla \cdot (n_c \mathbf{v}) \simeq -\lambda \Delta \mu, \quad (2.86)$$

since $|\partial \delta n_i / \partial t| / |\nabla \cdot (n_i \mathbf{v})| \sim \delta n_i / n_i$ which, as we just discussed in Sec. 2.1.2, must be of order of the magnetic-degeneracy pressure ratio $B^2 / 8\pi P \ll 1$. Thus, the characteristic fluid velocity is roughly

$$v \sim \frac{\lambda \Delta \mu}{n_c} L_c, \quad (2.87)$$

where $L_c \equiv |n_c \mathbf{v} / (\nabla \cdot (n_c \mathbf{v}))|$ is the characteristic length scale of the charged-particle flux. Therefore, the characteristic time-scale over which the magnetic field readjusts is given by

$$t_{\lambda B} \sim \frac{L}{v} \sim \frac{4\pi n_c^2}{\lambda B^2} \quad (2.88)$$

where we took the factor $L/L_c \sim 1$, which will be checked numerically in Chap. 4. Finally, we remark that, in order to satisfy the equations (2.85) and (2.86), the fluxes of neutrons and charged particles must have different characteristic length. For neutrons, it must be $L_n \approx \varepsilon L_c$ ($\varepsilon \equiv n_n(r=0)/n_c(r=0) \approx 10$), since the ratio is proportional to the quotient of the background densities (that is the reason we distinguish the length scales in this section). And, the ratio between these last two time-scales, t_λ and $t_{\lambda B}$, is roughly

$$\frac{t_\lambda}{t_{\lambda B}} \sim \frac{B^2}{4\pi n_c^2 (K_{cc} + K_{nn})} \sim \frac{B^2}{8\pi P}. \quad (2.89)$$

Therefore, $t_\lambda \ll t_{\lambda B}$, so that temperature should substantially evolve at $\sim t_{\lambda B}$.

Chapter 3

Numerical approach

In this chapter, we review some technical details of the numerical strategy we implemented. The chapter is organized as follows: In Sec. 3.1, we describe the method that allows us to add the effects of the evolution of the temperature into the evolution of the magnetic field, without having to re-run the latter. In Sec. 3.2, we write the equations to evolve the magnetic field and temperature separately in dimensionless units. Finally, we briefly outline the discretization of the polar grid we used and other numerical details already implemented in the code of [Castillo et al. \(2020\)](#).

3.1 Time parametrization

In [Castillo et al. \(2017\)](#) and [Castillo et al. \(2020\)](#), equations (2.22)-(2.32) were solved for the “weak coupling” regime ($\mathbf{v}_{ad} \neq 0$), where $\Delta\Gamma = 0$, and γ_{cn} are independent of time (i.e., at constant, low temperature). However, these quantities do depend on the internal temperature, and the evolution of the latter can strongly affect the dynamics. Therefore, our purpose is to take this into account for the “strong coupling” regime ($\mathbf{v}_{ad} = 0$; $\Delta\Gamma \neq 0$), where the temperature dependence appears only in $\Delta\Gamma$. In the “subthermal” approximation ($\Delta\Gamma = \lambda\Delta\mu$), the available phase space for mUrca reactions is determined only by temperature and its dependence can be separated from the particle emission rate (see equation [2.66]). This allows us to introduce the temperature dependence through a change in the time variable, $t \rightarrow t'$, from the real physical situation, where temperature evolves (with the variable t), to the non-physical case at constant temperature (with the variable t'). Thus, performing this change of variable,

the induction, velocity, and continuity equations read as follows:

$$\frac{\partial \mathbf{B}}{\partial t'} = \nabla \times (\mathbf{v}' \times \mathbf{B}), \quad (3.1)$$

$$\mathbf{v}' \frac{dt'}{dt} = \frac{1}{\zeta n_n} (\mathbf{f}_B + \mathbf{f}_c + \mathbf{f}_n), \quad (3.2)$$

$$\frac{dt'}{dt} \left[\frac{\partial \delta n_i}{\partial t'} + \nabla \cdot (n_i \mathbf{v}') \right] = \pm \lambda(T_0) \left(\frac{T}{T_0} \right)^6 \Delta \mu, \quad i = c, n, \quad (3.3)$$

where we have explicitly written the temperature dependence of λ in terms of the initial temperature T_0 . By assuming that the inverse of the fictitious friction parameter has the same dependence on temperature as λ , i.e. $\zeta = \zeta(T_0)(T/T_0)^{-6}$, one may choose

$$\frac{dt'}{dt} \equiv \left(\frac{T}{T_0} \right)^6, \quad (3.4)$$

so that equations (3.1)-(3.3) become temperature-independent:

$$\frac{\partial \mathbf{B}}{\partial t'} = \nabla \times (\mathbf{v}' \times \mathbf{B}), \quad (3.5)$$

$$\mathbf{v}' = \frac{1}{\zeta(T_0) n_n} (\mathbf{f}_B + \mathbf{f}_c + \mathbf{f}_n), \quad (3.6)$$

$$\frac{\partial \delta n_i}{\partial t'} + \nabla \cdot (n_i \mathbf{v}') = \pm \lambda(T_0) \Delta \mu, \quad i = c, n. \quad (3.7)$$

Therefore, our approach can be understood as follows:

1. We run the simulations using the code of [Castillo et al. \(2020\)](#), and assume the time variable corresponds to t' .
2. Then, using these results, we solve the equation for the temperature

$$\frac{dT}{dt'} = \frac{1}{C} \left[\mathcal{L}'_{\zeta} - \frac{1}{2} \mathcal{L}'_{\text{H}\nu} - \mathcal{L}^{*\prime}_{\nu} \left(\frac{T}{T_0} \right)^2 \right], \quad (3.8)$$

where we replaced $\mathcal{L}_{\zeta} = \mathcal{L}'_{\zeta} (T/T_0)^6$, $\mathcal{L}_{\text{H}\nu} = \mathcal{L}'_{\text{H}\nu} (T/T_0)^6$, and $\mathcal{L}_{\nu}^* = \mathcal{L}^{*\prime}_{\nu} (T/T_0)^8$. We finally obtain the physical time variable that includes the effects of the temperature evolution,

$$t = \int_0^{t'} \left(\frac{T}{T_0} \right)^{-6} dt'. \quad (3.9)$$

Thus, we can plot any variable of interest as a function of t .

Finally, we recall that this procedure is feasible because in the ‘‘subthermal’’ regime, the temperature dependence can be separated in λ , and this would not be possible for the most general situation when all the terms in equation (2.57) are considered.

3.2 Dimensionless equations

The equations to be solved numerically have been written in dimensionless form for the “strong-coupling” regime with the time variable t' ,

$$\frac{\partial \alpha}{\partial t'} = -\mathbf{v}' \cdot \nabla \alpha, \quad (3.10)$$

$$\frac{\partial \beta}{\partial t'} = r^2 \sin^2 \theta \nabla \cdot \left(\frac{(\mathbf{v}' \times \mathbf{B}) \times \hat{\phi}}{r \sin \theta} \right), \quad (3.11)$$

$$\frac{\partial \delta n_n}{\partial t'} + \nabla \cdot (n_n \mathbf{v}') = +\lambda(T_0) \Delta \mu, \quad (3.12)$$

$$\frac{\partial \delta n_c}{\partial t'} + \nabla \cdot (n_c \mathbf{v}') = -\lambda(T_0) \Delta \mu, \quad (3.13)$$

$$\mathbf{v}' = \frac{\varepsilon}{\zeta(T_0) n_n} \left[b^2 (\nabla \times \mathbf{B}) \times \mathbf{B} - n_n \mu \nabla \left(\frac{\delta \mu_n}{\mu} \right) - n_c \mu \nabla \left(\frac{\delta \mu_c}{\mu} \right) \right], \quad (3.14)$$

$$\frac{dT}{dt'} = \frac{\Lambda}{T} \left(\mathcal{L}'_\zeta - \frac{1}{2} \mathcal{L}'_{H\nu} - \eta \mathcal{L}'_\nu T^2 \right) \quad (3.15)$$

$$\delta \mu_c = K_{cc} \delta n_c, \quad (3.16)$$

$$\delta \mu_n = K_{nn} \delta n_n, \quad (3.17)$$

where distances have been normalized in the code to the radius R of the core, number densities δn_n and δn_c are in units of n_{c0} , K_{nn} and K_{cc} are in units of $K_{cc0} = K_{cc}(r=0)$, γ_{cn} is in units of $\gamma_{cn0} = \gamma_{cn}(r=0, T=10^8 \text{K})$, time has been normalized to $t_0 = R^2 \gamma_{cn0} / K_{cc0}$, chemical potentials are in units of $K_{cc0} n_{c0}$, ζ is in units of $\gamma_{cn0} n_{c0}$, velocities are normalized to $v_0 = R/t_0$, λ is in units of $(\gamma_{cn0} R^2)^{-1}$, luminosities are in units of $\mathcal{L}_0 = K_{cc0} n_{c0}^2 R^3 / t_0$, and the magnetic field is in units of B_0 (the root mean square of the magnetic field in the volume of the star). Temperature is in units of the initial temperature T_0 . α and β are in units of $R^2 B_0$ and RB_0 , respectively. The constants in the temperature equation are $\Lambda = \mathcal{L}_0 t_0 / [C(T_0) T_0]$ and $\eta = \mathcal{L}'_\nu(T_0) / \mathcal{L}_0$, respectively. We control the strength of the magnetic field adjusting the parameter

$$b^2 \equiv \frac{B_0^2}{4\pi K_{cc0} n_{c0}^2}, \quad (3.18)$$

which is of the order of the (very small) ratio between the magnetic and charged-particle degeneracy pressure. Thus, $B_0 = n_{c0} \sqrt{4\pi K_{cc0}} b \sim 2 \times 10^{18} bG$ for the star we are using ($n_{c0}/n_{n0} = 0.1$). Hereafter we take the values of the different time-scales at the center of the NS as reference values, which in dimensionless

units read, from the shortest to the longest,

$$t'_{\zeta p} = \frac{K_{cc}n_c^2}{K_{nn}n_n^2} \Big|_{r=0} \zeta(T_0)x^2 = \frac{\zeta(T_0)x^2}{16.45}, \quad (3.19)$$

$$t'_{\zeta g} = \zeta(T_0)x^2, \quad (3.20)$$

$$t'_{\zeta B} = \frac{\zeta(T_0)x^2}{b^2}, \quad (3.21)$$

$$t'_{\text{chem}} = \frac{1}{\lambda(T_0)b^2}, \quad (3.22)$$

where we have taken $x \equiv L/R = 1/4$. In order to properly resolve all four time-scales in our simulations without having to use a prohibitively small time-step, we scale the values of the magnetic field (fixed by b), and ζ , so that the four time-scales get closer to each other. The code evolves the set of equations (3.10)–(3.14) at constant temperature, and equation (3.15) must be solved separately from the output results. In the code, the values of the variables are discretized over a staggered polar grid composed of N_r points inhomogeneously distributed in the radial direction inside the core (see Fig. (3.1)) and N_θ points equally spaced in the polar direction. The points are placed in spherical coordinates at

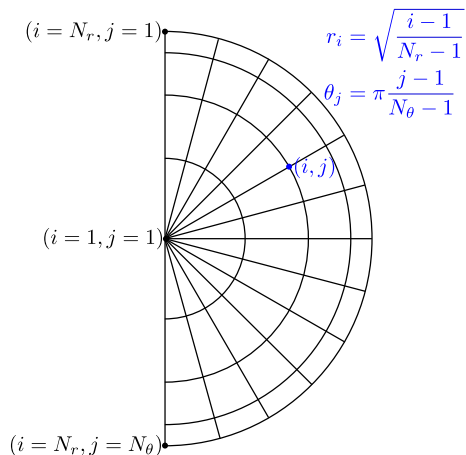


Figure 3.1: Spherical grid used to spatially discretize the code variables.

$$r_i = \sqrt{\frac{i-1}{N_r-1}}, \quad (3.23)$$

$$\theta_j = (j-1)\Delta\theta, \quad (3.24)$$

where $i = 1, \dots, N_r$; $j = 1, \dots, N_\theta$ and $\Delta\theta = \pi/(N_\theta - 1)$. On the other hand, the external multipolar expansion is truncated to the first N_{Exp} terms. The numerical computation is done conservatively for the evolution of the toroidal

magnetic field and the density perturbations of the charged particles and neutrons, using a finite volume scheme. The time derivative of the poloidal potential is computed using finite difference, and the system is evolved to second-order accuracy in time. This scheme guarantees that the condition $\nabla \cdot \mathbf{B} = 0$, as well as the total number of particles, are conserved at all times to machine precision. (Further details on the numerical code can be seen in [Castillo et al. 2017](#).)

Chapter 4

Results

In this chapter we present the results of the magneto-thermal evolution in the “strong-coupling regime”. The chapter is organized as follows: In Sec. 4.1, we discuss the results at constant temperature, in terms of the non-physical time variable t' . First, we check the dependence of our simulations on the fictitious friction parameter $\zeta(T_0)$. Then, we analyse the short-term hydro-magnetic and long-term magneto-chemical equilibria. We discuss the force balance throughout the evolution and check when the continuity equations are stationary (equation [2.85] and [2.86]). Afterwards, we study the magnetic energy dissipation (equation [2.48]) and the final “Grad-Shafranov” equilibrium state. In Sec. 4.2, we present the results where temperature evolution is taken into account, i.e. in terms of the physical time variable t , outlining the main differences with the previous case. Later, we present a plausible way to scale our results down to a magnetar-like internal field, $B \sim 10^{16}$ G. And finally, we explore the possibility of having a magnetic feedback on the internal temperature due to mUrca reactions.

4.1 Constant temperature

4.1.1 Dependence on the artificial friction

The fictitious force \mathbf{f}_ζ allows initial configurations with an arbitrary particle densities and magnetic field to reach a hydromagnetic quasi-equilibrium on a time-scale $\sim t'_{\zeta B}$, much shorter than the one of interest for the long-term evolution of the magnetic field (Castillo et al., 2020). We choose the ratio $t'_{\zeta B}/t'_{\lambda B}$ not realistically, but instead, small enough for a feasible numerical simulation, so that a significant fraction of the evolution $t'_{\zeta B} < t' < t'_{\lambda B}$ can be studied. This implies that the friction parameter ζ cannot be arbitrary and the results for the long-term evolution must be independent of its value. We follow the same procedure of Castillo et al. (2020) to determine the appropriate value of $\zeta(T_0)$; since the total integration time is proportional to $t'_{\lambda B}/t'_{\zeta p} = 0.36/\zeta(T_0)b^2$, decreasing the values of $\zeta(T_0)$ and b , increases the integration time very quickly. Thus, we perform a test with an unrealistically large value of b^2 , namely 3×10^{-2} , and for ζ we took three different values $\zeta(T_0) = 10^{-3}$, 10^{-4} , and 10^{-5} , which yield the ratios $t'_{\lambda B}/t'_{\zeta B} = 22$, 220, and 2200, respectively. These values of $\zeta(T_0)$ are a factor 52, 520, and 5200 smaller than $n_c^2/\lambda n_n L_c^2$, so the condition in equation (2.78), for $L_c \sim 1$ km (see Sec.4.1.3), is fulfilled. For all the following results (at constant and variable temperate), we choose as initial condition, the magnetic field generated by the potential

$$\alpha(r, \theta) = \sqrt{0.23}\alpha_1(r, \theta) + \sqrt{0.47}\alpha_2(r, \theta), \quad (4.1)$$

where

$$\alpha_1(r, \theta) = \alpha_{01} \left(1 - \frac{6}{5}r^2 + \frac{3}{7}r^4 \right) r^2 \sin^2 \theta, \quad (4.2)$$

$$\alpha_2(r, \theta) = \alpha_{02} \left(1 - \frac{10}{7}r^2 + \frac{5}{9}r^4 \right) r^3 \sin^2 \theta \cos \theta, \quad (4.3)$$

and, $\alpha_{01} = 0.567$ and $\alpha_{02} = 2.409$, are normalization constants fixed by the condition $\langle \mathbf{B}_{\text{pol}} \rangle = 1$. The toroidal potential is given by

$$\beta(r, \theta) = \sqrt{0.3}\beta_1 r^6 (1 - r)^2 \sin^2 \theta \sin(\theta - \pi/5), \quad (4.4)$$

and the constant $\beta_1 = 151.382$ is fixed by the condition $\langle \mathbf{B}_{\text{Tor}} \rangle = 1$. The numbers in square roots are chosen so that 30% of the initial magnetic energy is toroidal. In the following simulations (at constant and variable temperature), we shall also use the same number of grid points, N_r and N_θ , and external multipoles N_{Exp} .

The results are summarized in Fig. 4.1. Panel (a) shows that during the early stages ($\lesssim t'_{\zeta B}$), the magnetic field readjusts and then slowly evolves over the longer times-scales $\sim t'_{\lambda B}$. The artificial friction dominates the dynamics at the early stages of the evolution, and then each curve starts to converge to its asymptotic value for $t' \gtrsim t'_{\zeta B}$. Panels (b) and (c) show the convergence of \mathbf{v}' and

$\Delta\mu$, for simulations with very different values of ζ , so we are indeed obtaining the expected results, namely $f_\zeta \propto \zeta$, and $\Delta\mu \sim B^2/4\pi n_c \sim 3 \times 10^{-2}$ as its maximum value (in code units $\mu_0 = 4 \times 10^{-4}$ erg), reproducing the correct “physical” fluid velocity and magneto-chemical evolution on time-scales $t' > t'_{\zeta B}$ independent of the value used for ζ . The good agreement of the three curves after this time suggests that all three values chosen for ζ are adequate for our purpose. To be on the safe side, we will use $\zeta(T_0) = 10^{-4}$ to proceed with further analysis, and not $\zeta(T_0) = 10^{-5}$ because of numerical limitations (making $\zeta(T_0)$ one order of magnitude smaller increases the integration time by the same factor).

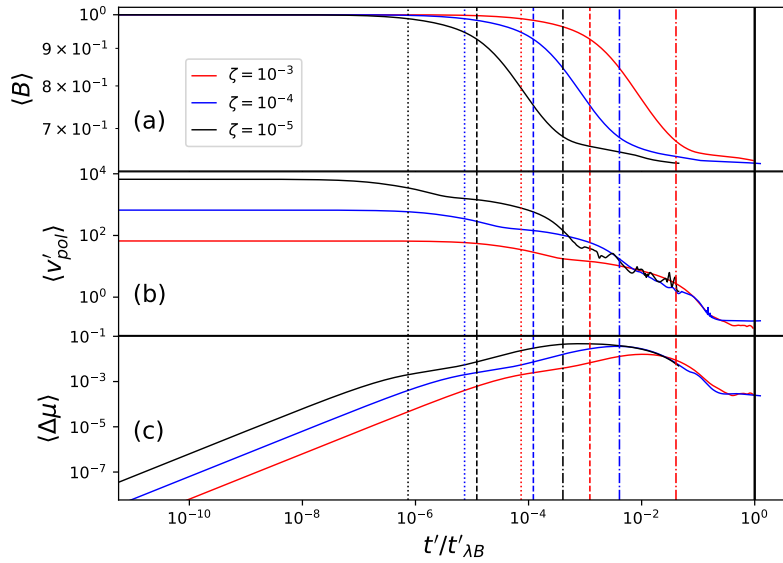


Figure 4.1: Comparison of the evolution of simulations using the same initial condition, equations (4.1) to (4.4), at constant temperature $T = 3 \times 10^9$ K, and three very different values of ζ (10^{-3} , red; 10^{-4} , blue, and 10^{-5} , black), with the following ratios between the different relevant time-scales at the center of the star; $t'_{\zeta p} : t'_{\zeta g} : t'_{\zeta B} : t'_{\lambda B} = 1 : 16.5 : 548 : 12038$, $t'_{\zeta p} : t'_{\zeta g} : t'_{\zeta B} : t'_{\lambda B} = 1 : 16.5 : 548 : 120384$ and $t'_{\zeta p} : t'_{\zeta g} : t'_{\zeta B} : t'_{\lambda B} = 1 : 16.5 : 548 : 1203840$, respectively. The vertical lines show the values of all the time-scales with their respective color for the different ζ of each simulation. We used a grid of $N_r = 60$ radial steps and $N_\theta = 91$ polar steps inside the core, as well as $N_{Exp} = 27$ external multipoles. The panels show the time evolution of: (a) the magnetic field $\langle B \rangle$ in units of B_0 , (b) the poloidal component of the fluid velocity $\langle v_{pol} \rangle$, and (c) chemical imbalance $\langle \Delta\mu \rangle$. Here, $\langle \cdot \rangle$ denotes the root mean square (rms) average in the volume of the core.

4.1.2 Hydro-magnetic and magneto-chemical evolution

During the short time-scale $t_{\zeta p}$, there are quick adjustments of the densities because the magnetic field pushes the fluid, forcing the growth of the perturbations $\delta n_n(r, \theta)$ and $\delta n_c(r, \theta)$ with similar structure, in particular the same sign over almost the whole NS volume. This can be seen in the second row of Fig. 4.2, where different snapshots of the magnetic field, fractional density perturbations, poloidal velocity field and the source of the equations of continuity are shown. At later times ($\gtrsim t'_{\zeta g}$), neutrons and charged particles behave differently because the non-trivial poloidal velocity field $\mathbf{v}'^{\text{Pol}}(r, \theta)$ and the background density profile ($n_n(r)/n_c(r) \neq \text{constant}$) grow perturbations with not necessarily the same signs, allowing their different fluid forces to jointly balance both components of the poloidal magnetic force. Thus, in the following stages of the evolution, the velocity field behaves as a stably stratified and non-barotropic fluid (because the system is still far away from chemical equilibrium). We remark that these time-scales, $t'_{\zeta p}$ and $t'_{\zeta g}$, are much shorter than the time-scales for magnetic field evolution, therefore, the magnetic field remains unchanged during these processes, as can be seen in the column (a) in Fig. 4.2. In the fourth row (at $t'_{\zeta B}$), the magnetic field unwinds, eliminating most of the toroidal component, except in the regions of closed poloidal field lines, reaching the “twisted-torus” configurations expected in axially symmetric hydromagnetic equilibria (Pren-dergast, 1956; Braithwaite & Spruit, 2004)

On a much longer time-scale ($\lesssim t'_{\lambda B}$), mUrca reactions operate, slowly eroding the equilibrium reached at $t'_{\zeta B}$. The conversion of neutrons to charged particles and vice versa requires the magnetic field to slowly rearrange moving charged particles (and neutrons) so the evolution proceeds through a continuum of consecutive quasi-equilibrium steps. At this stage, further fluid displacements keep maintaining $\mathbf{f}_B + \mathbf{f}_c + \mathbf{f}_n \simeq 0$ and eventually lead to a final magneto-chemical equilibrium where $\mathbf{v}' \simeq 0$ and $\Delta\mu \simeq 0$. In the last row of the figure (at $t'_{\lambda B}$), one can see that the source term approaches zero, though it is affected by numerical noise at the center. The velocity field, obtained from the quotient of the force imbalance and ζn_n , is small but noisy because of truncation error in the quasi-cancellation of forces, suggesting that the final magneto-chemical equilibrium has been reached. Moreover, the fractional density perturbation reaches a final value $|\delta n_i|/n_i \sim b^2$ ($i = c, n$), which is the expected result (see the fifth row in Fig. 4.2).

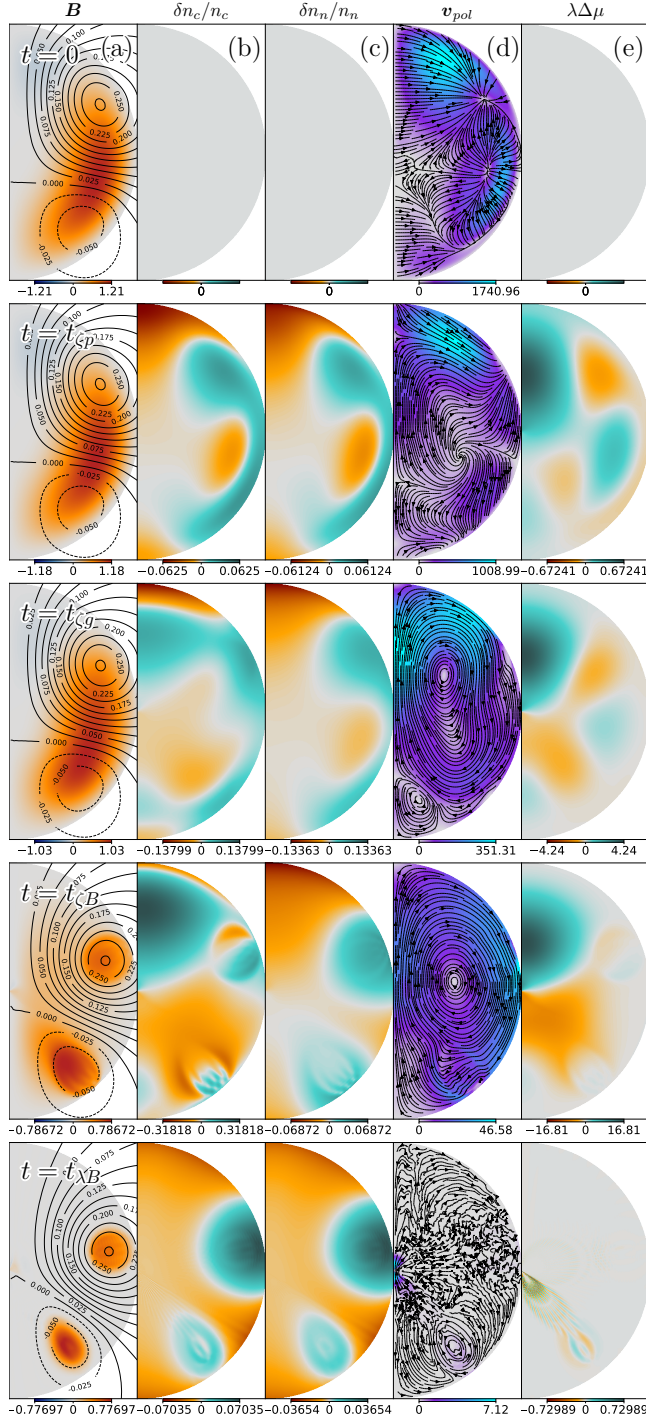


Figure 4.2: Evolution of the magnetic field for the simulation shown in Fig. 4.1 with $\zeta = 10^{-4}$. From left to right: (a) Configuration of the magnetic field, where lines represent the poloidal magnetic field (labeled by the magnitude of α) and colors the toroidal potential β ; (b) and (c) the fractional density perturbations $\delta n_c/n_c$ and $\delta n_n/n_n$, respectively; (d) the poloidal component of the velocity field, \mathbf{v} , normalized to R/t_0 and (e) net emission rate in units of $\lambda_0 \mu_0$. Rows correspond to different times: $t' = 0, t'_{\zeta p}, t'_{\zeta p}, t'_{\zeta B}$, and $t'_{\lambda B}$.

4.1.3 Force balance and continuity equations

The strength of the magnetic and fluid forces throughout the simulation can be followed in Fig. 4.3. At early stages ($< t'_{\zeta P}$), the poloidal Lorentz force is balanced by $\mathbf{f}_{\zeta}^{\text{Pol}}$, meanwhile the bulk motions grow the gradient forces decreasing $\mathbf{f}_{\zeta}^{\text{Pol}}$. Later ($\sim t'_{\zeta P}$), the poloidal magnetic force is partially balanced by the fluid force of the neutrons, while the contribution of the charged particles is much smaller¹. This is because at this stage the charged particles and neutrons, at any point in the star, are jointly compressed or expanded by the magnetic force (with $\delta n_c/n_c \sim \delta n_n/n_n$) and, since there are many more neutrons than charged particles present, they represent the main contribution to the pressure of the fluid. At later times, $t'_{\zeta g} < t' < t'_{\zeta B}$, the contribution of both degeneracy forces indeed jointly balance $\mathbf{f}_B^{\text{Pol}}$, as we just discussed in the previous section.

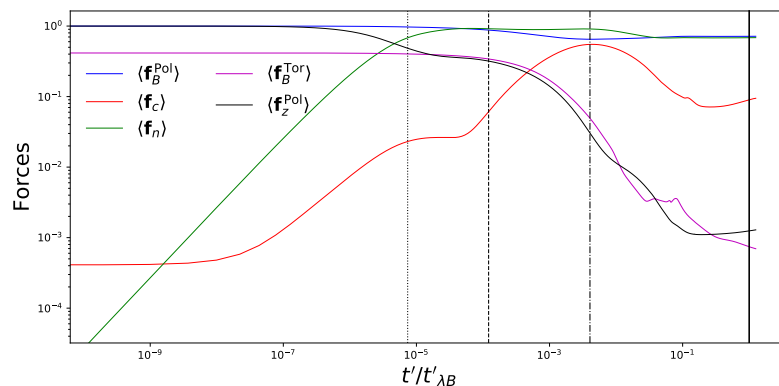


Figure 4.3: Time evolution of the force balance for the simulation with $\zeta = 10^{-4}$ in Fig. 4.1: $\langle \mathbf{f}_B^{\text{Pol}} \rangle$, $\langle \mathbf{f}_B^{\text{Tor}} \rangle$, $\langle \mathbf{f}_n \rangle$, $\langle \mathbf{f}_c \rangle$, and $\langle \mathbf{f}_{\zeta}^{\text{Pol}} \rangle$ normalized to $\langle \mathbf{f}_B^{\text{Pol}}(t=0) \rangle$, where $\langle \cdot \rangle$ denotes the rms average over the NS volume. The vertical lines show, from left to right, the values of the time-scales $t'_{\zeta P}$, $t'_{\zeta g}$, $t'_{\zeta B}$ and $t'_{\lambda B}$.

At $t'_{\zeta B}$, the poloidal magnetic force and pressure forces are all of the same order, and the poloidal force imbalance $\mathbf{f}_{\zeta}^{\text{Pol}}$ is much smaller. This means that, in the poloidal component, there is indeed a balance between the magnetic and the induced fluid forces. On the other hand, the toroidal component of the Lorentz force, which reads as

$$\mathbf{f}_B^{\text{Tor}} = \frac{\nabla \beta \times \nabla \alpha}{4\pi}, \quad (4.5)$$

is by construction balanced by the fictitious force, i.e., $\mathbf{f}_B^{\text{Tor}} = \mathbf{f}_{\zeta}^{\text{Tor}}$, because there is no toroidal pressure gradient or gravitational force available to balance

¹The initial charged-particle force is not zero because, due to the boundary conditions (equations [2.34] to [2.35]), it must compensate the radial Lorentz force at the boundary.

a toroidal component of the Lorentz force. Therefore, a necessary equilibrium condition in axial symmetry is $\mathbf{f}_B^{\text{Tor}} = 0$ or equivalently $\nabla\alpha \parallel \nabla\beta$, which imposes the restriction that one potential is a function of the other, i.e.

$$\beta = \beta(\alpha), \quad (4.6)$$

(although this function might not be single-valued). At $\sim t'_{\zeta B}$, it can be seen that $\mathbf{f}_B^{\text{Tor}}$ is indeed much smaller than the other forces, so the condition (4.6) is fulfilled (see also Fig. 4.6). The quasi-equilibrium reached at $t'_{\zeta B}$, leads to an excess of charged-particle perturbations in order to keep $\mathbf{f}_B + \mathbf{f}_c + \mathbf{f}_n \approx 0$ (see the fourth row in Fig. 4.2). This excess is erased by mUrca reactions as the star approaches chemical equilibrium (at $\sim t'_{\lambda B}$) by decreasing δn_c , i.e., by converting more charged particles to neutrons. This explains why the chemical imbalance decreases from its maximum value since $\Delta\mu = K_{cc}\delta n_c - K_{nn}\delta n_n$. On the other hand, while reaching chemical equilibrium ($\delta\mu_c \approx \delta\mu_n$), the particle gradient forces, \mathbf{f}_n and \mathbf{f}_c , start to become parallel. Therefore, at the final state, the core matter behaves as a barotropic fluid at chemical equilibrium, where most of the poloidal Lorentz force $\mathbf{f}_B^{\text{Pol}}$ is balanced by the neutron pressure force \mathbf{f}_n . Finally, we remark that the artificial forces $\mathbf{f}_\zeta^{\text{Pol}}$ and $\mathbf{f}_\zeta^{\text{Tor}}$, play no significant role in the magnetic field evolution at the final stages.

The quotients of the terms in the continuity equations, (2.72) and (2.73), are shown in rms-average in Fig. 4.4. At early stages ($< t'_{\zeta g}$), the time derivatives of the number density perturbations are of the same order as the divergences but much smaller than the source terms, as can be seen in panels (b) and (c). This is expected because at this stage perturbations and the chemical imbalance are growing by the quick initial bulk motions. Later (at $\sim t'_{\zeta B}$), there is a local minimum in the quotient $|\partial\delta n_c/\partial t'|/|\nabla \cdot (n_c \mathbf{v}')|$, which coincides with the maximum of $|\Delta\mu|$ and suggests that the quasi-equilibrium, where $\mathbf{f}_B + \mathbf{f}_c + \mathbf{f}_n \approx 0$, is reached. At the final stage ($\sim t'_{\lambda B}$), the magnitude of the time derivatives is roughly $|\partial\delta n_c/\partial t'| \sim |\delta n_c|/t'_{\lambda B} \sim b^2\lambda|\Delta\mu|(L_v/L)$, and $|\partial\delta n_n/\partial t'| \sim \varepsilon|\partial\delta n_c/\partial t'|$ ($\varepsilon = n_n(r=0)/n_c(r=0) \approx 10$). Thus, the quotient $|\partial\delta n_c/\partial t'|/\lambda|\Delta\mu| \sim b^2(L_v/L) \sim 3 \times 10^{-2}(L_v/L)$, which is in good agreement with the results shown in panel (c), and the initial assumption, $L_v/L \sim 1$, also seems to be valid. It is easy to check that the quotient $|\partial\delta n_c/\partial t'|/|\nabla \cdot (n_c \mathbf{v}')|$ is equivalent to the former, and panel b) shows that this result is also in good agreement, however, this quotient is much larger at the first time-scales ($\lesssim t'_{\zeta g}$) because $\Delta\mu(t' \simeq 0) \simeq 0$. Panel (a) shows that the ratio $\langle \nabla \cdot (n_c \mathbf{v}') \rangle / \langle \nabla \cdot (n_n \mathbf{v}') \rangle$ is equal to one at the final stages of the evolution, so the equations (2.85) and (2.86) hold, i.e., the continuity equations are stationary. At the final stages ($\sim t'_{\lambda B}$), the velocity field must be given by the particle conversion rate, $v'_{\text{pol}} \sim \lambda\Delta\mu L_c/n_c$, so the quotient $v'_{\text{pol}}/\lambda\Delta\mu$ must be constant and of order $\sim L_c/n_c$, which in code units is $\sim 1 (L_c/1 \text{ km})$, very similar to the result shown in panel (d). Finally, when considering the temperature evolution, each term in the continuity equations must be multiplied by a factor $(T/T_0)^6$, so the quotients do not change and these results still hold. However, the only difference will be in the time axis, when mapping the final the final time-scale, $t'_{\lambda B} \rightarrow t_{\lambda B}$, through the equation (3.9) (see Sec. 4.2 for more details).

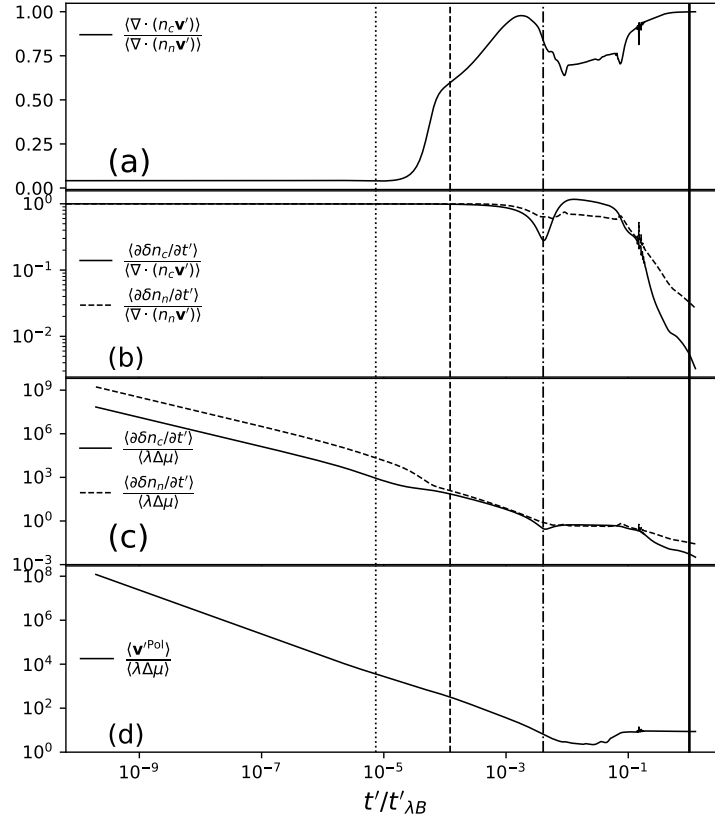


Figure 4.4: Terms of the continuity equations for the simulation with $\zeta = 10^{-4}$; (a) shows the time evolution of the quotient $\langle \nabla \cdot (n_c \mathbf{v}') \rangle / \langle \nabla \cdot (n_n \mathbf{v}') \rangle$, (b) shows the quotient of $\langle \partial \delta n_n / \partial t' \rangle / \langle \nabla \cdot (n_n \mathbf{v}') \rangle$ (dashed) and $\langle \partial \delta n_c / \partial t' \rangle / \langle \nabla \cdot (n_c \mathbf{v}') \rangle$ (solid), (c) shows $\langle \partial \delta n_n / \partial t' \rangle / \langle \lambda \Delta \mu \rangle$ (dashed) and $\langle \partial \delta n_c / \partial t' \rangle / \langle \lambda \Delta \mu \rangle$ (solid), and (d) shows the quotient $\langle v'_{pol} \rangle / \langle \lambda \Delta \mu \rangle$, where $\langle \cdot \rangle$ denotes the rms average over the NS core. The vertical lines show, from left to right, the values of the time-scales $t'_{\zeta p}$, $t'_{\zeta g}$, $t'_{\zeta B}$ and $t'_{\lambda B}$.

4.1.4 Energy dissipation

Before proceeding with the discussion, an important remark is that our scheme is not completely conservative because we used the effective mass for particles (chemical potential) instead of the real one, and we have done several simplifications when truncating the redshift factor, e^{Ψ/c^2} , to obtain the magnetic energy dissipation expression (equation [2.48]). Fig. 4.5 shows in panel (a) all the terms in equation (2.48) multiplied by time, corresponding to the energy dissipated in equal intervals of $\ln t'$, and allows to check better the results at the time-scales of interest. In panel (b), we show the terms $\mathcal{L}'_{H\nu}$, $\mathcal{L}'_{\zeta}{}^{\text{Pol}}$, and $\mathcal{L}'_{\zeta}{}^{\text{Tor}}$ multiplied by t' for two different values of $\zeta(T_0)$. As expected, initially the dynamics is given by quick fluid motion with velocity $\mathbf{v}' \sim \mathbf{f}_B^{\text{Pol}}/\zeta(T_0)n_n$, and the fictitious friction dominates, scaling as $\mathcal{L}'_{\zeta} \propto \zeta(T_0)^{-1}$, so it is larger for $\zeta(T_0) = 10^{-4}$ than for $\zeta(T_0) = 10^{-3}$, as seen in panel (a). At the final stages, the velocity field becomes independent of $\zeta(T_0)$ (see Fig. 4.1), therefore, the friction term should scale as $\mathcal{L}'_{\zeta} \propto \zeta(T_0)$. However, if that is true, this term should not be relevant because, with $\zeta(T_0) = 10^{-3}, 10^{-4}$, the condition in equation (2.78) is fulfilled. Sadly, this term still dominates because the toroidal part, $\mathcal{L}'_{\zeta}{}^{\text{Tor}} \propto (\nabla\beta \times \nabla\alpha)^2$ (larger than $\mathcal{L}'_{\zeta}{}^{\text{Pol}}$, as can be seen in the panel (b)), is affected by a problem of numerical precision since it is computed from the cross product of two almost parallel vectors (see also Fig. 4.6) at the final stages.

A natural way to avoid this problem is to chose an even smaller value of $\zeta(T_0)$. This would be more realistic but less numerically feasible, so we proceed to elucidate what would happen with a more realistic $\zeta(T_0)$ using the results we already have. We might understand this physically as follows: Let us consider the toy model of a horizontal magnetic flux in a degenerate gas of neutrons, protons, and electrons that rises due to magnetic buoyancy (following the reasoning of Reisenegger (2009) [section 3.3]). Similarly to our previous discussion, if the flux was held at its initial position, it would quickly reach chemical equilibrium at a time-scale $\sim t'_{\lambda}$, however, mUrca reactions increase the pressure inside the flux, so the tube rises to a new hydrostatical equilibrium in a longer time-scale $\sim t'_{\lambda B}$. Now, the effect of the fictitious frictional drag force, $\zeta n_n \mathbf{v}$, is to delay the flux rising, dissipating part of the energy as the tube reaches chemical equilibrium. In other words, for smaller values of ζ , the NS core remains out of chemical equilibrium for a longer time (i.e., $t'_{\lambda B} \gg t'_{\zeta B}$, see also $\Delta\mu$ in Fig. 4.1) and more energy is dissipated by the term $\mathcal{L}'_{H\nu}$ instead of \mathcal{L}'_{ζ} , as can be seen in panel (b). Therefore, one may conclude that for a realistic value of ζ the effect of \mathcal{L}'_{ζ} should be negligible compared with $\mathcal{L}'_{H\nu}$ at the physical time-scales $\sim t'_{\lambda B}$ because of energy conservation.

Another interesting fact of our simulations comes from the Poynting flux shown in panel (a). The negative sign of \mathcal{L}'_p , respect to the other terms, is because we do not have an atmosphere where currents could be dissipated, leaving the current-free field that we are imposing with the boundary conditions. Instead, the magnetic energy is injected into the NS core (although a small amount compared with the other terms). One could have expected this because

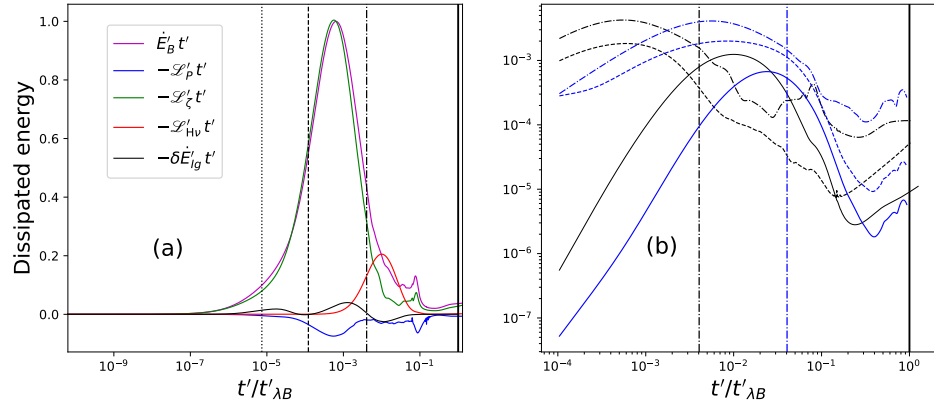


Figure 4.5: Magnetic energy dissipation; (a) for the simulation with $\zeta = 10^{-4}$ in Fig. 4.1; each term in the equation (2.48) multiplied by time and normalized to the maximum value of $\dot{E}'_B t'$. In pink the time derivative of the magnetic energy, in blue the Poynting flux, in green the dissipation by the artificial friction force, in red the chemical energy released, and in black the internal energy enhancement. (b) for the simulations with $\zeta = 10^{-4}$ (black), and $\zeta = 10^{-3}$ (blue) in Fig. 4.1; $\mathcal{L}'_{\zeta}{}^{\text{Tor}} t'$ (dash-dotted), $\mathcal{L}'_{\zeta}{}^{\text{Pol}} t'$ (dashed) and $\mathcal{L}'_{H\nu} t'$ (solid). The vertical lines show in (a), from left to right, the values of the time-scales $t'_{\zeta p}$, $t'_{\zeta g}$, $t'_{\zeta B}$ and $t'_{\lambda B}$, respectively; and in (b) only the time-scales $t'_{\zeta B}$, and $t'_{\lambda B}$ with their respective color.

the physics is analogous to a wire carrying an electric current inside. Since most of the magnetic energy is located outside and the dissipation takes place inside, there must be a flux of magnetic energy from outside into the wire.

4.1.5 Grad-Shafranov equilibria

The results show that at $\sim t'_{\zeta B}$ the hydromagnetic quasi-equilibrium is reached and all the forces are close to balance. This implies that the toroidal magnetic force must vanish, so the condition in equation (4.6) must hold (at least locally). One can check this in Fig. 4.6, where at early times ($t'_{\zeta g}$) there is no clear relation between the variables, but at $\sim t_{\zeta B}$ there is an evident dependence of β on α .

At later times ($\sim t'_{\lambda B}$), the velocities become much smaller than their initial value, so the system is approaching a final equilibrium state where $\mathbf{v}' = 0$, and \mathbf{f}_{ζ} should be already negligible at this stage. This requires

$$\begin{aligned} \mathbf{v}'_{pol} &= \frac{1}{\zeta(T_0)n_n} \left[-\frac{1}{4\pi r^2 \sin^2 \theta} (\Delta^* \alpha \nabla \alpha + \beta \nabla \beta) - n_c \mu \nabla \chi_c - n_n \mu \nabla \chi_n \right] \\ &= 0, \end{aligned} \quad (4.7)$$

so the Lorentz force is balanced by the degeneracy pressure forces. Here, $\chi_c \equiv \delta\mu_c/\mu$ and $\chi_n \equiv \delta\mu_n/\mu$, and

$$\begin{aligned} \Delta^* &\equiv r^2 \sin^2 \theta \nabla \cdot \left(\frac{\nabla}{r^2 \sin^2 \theta} \right) \\ &= \frac{\partial^2}{\partial r^2} + \frac{\sin \theta}{r^2} \frac{\partial}{\partial \theta} \left(\frac{1}{\sin \theta} \frac{\partial}{\partial \theta} \right), \end{aligned} \quad (4.8)$$

is the ‘‘Grad-Shafranov (GS) operator’’. At $\sim t'_{\zeta B}$, the core fluid is out of chemical equilibrium, so there is no clear relation between χ_c , and χ_n , which can be verified in Fig. 4.6. However, at later times ($\sim t'_{\lambda B}$) the star approaches chemical equilibrium, $\delta\mu_c \approx \delta\mu_n$, so the gradient forces are parallel to $\nabla \alpha$. This last point also can be seen in Fig. 4.6, where there is an evident dependence on α for χ_c and χ_n , and the condition $\delta\mu_c = \delta\mu_n$ is achieved as discussed in Sec. 2.7 (it is most evident in the sixth row in panel (d), χ_n vs. χ_c). Taking this into account, equation (4.7) can be written as a ‘‘Grad-Shafranov (GS) equation’’ (Grad & Rubin, 1958; Shafranov, 1966):

$$\Delta^* \alpha + \beta \beta' + 4\pi r^2 \sin^2 \theta \mu(r) [n_n(r) \chi'_n + n_c(r) \chi'_c] = 0, \quad (4.9)$$

where β , χ_c , and χ_n are functions of $\alpha(r, \theta)$, and in principle $\chi_c = \chi_n$. Here primes denote derivatives with respect to α . We emphasize that (as seen in Fig. 4.6) this equation is generally not satisfied in the previous stage (at $\sim t'_{\zeta B}$), which is also a quasi-hydromagnetic equilibrium, but out of chemical equilibrium.

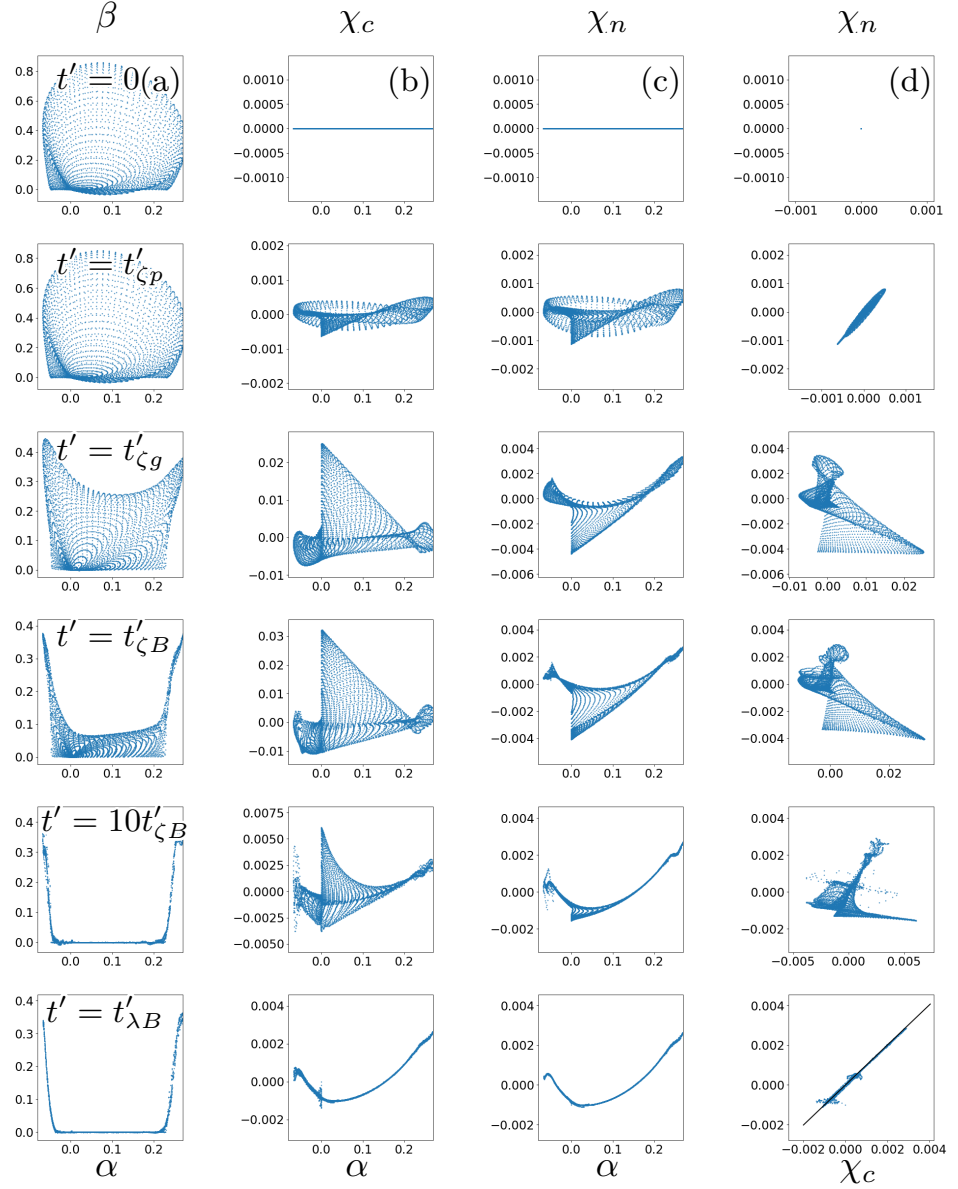


Figure 4.6: For the simulation with $\zeta = 10^{-4}$: Scatter plot of α versus (a) β , (b) χ_n , and (c) χ_c . In (d) χ_c versus χ_n , in the last figure we plot the identity function in black. We show the relation at all the grid points at $t' = 0, t'_{\zeta p}, t'_{\zeta g}, t'_{\zeta B}, 10t'_{\zeta B},$ and $t'_{\lambda B}$, respectively.

In order to check if our simulations lead to configurations in which the GS equation is satisfied at the expected time-scale ($\sim t'_{\lambda B}$), we evaluate the “GS integral” defined by

$$I_{GS} = \frac{\int_V d^3x |\Delta^* \alpha + \beta \beta' + 4\pi r^2 \sin^2 \theta \mu(r) [n_n(r) \chi'_n + n_c(r) \chi'_c]|}{V |\max \Delta^* \alpha|} \quad (4.10)$$

where the derivatives with respect to α are computed from our simulations taking $\beta' = (\nabla \beta \cdot \nabla \alpha) / |\nabla \alpha|^2$ and $\chi'_i = (\nabla \chi_i \cdot \nabla \alpha) / |\nabla \alpha|^2$, ($i = c, n$). Fig. 4.7 and Fig. 4.1 show that, in the time interval between $t'_{\zeta B}$ and $t'_{\lambda B}$, I_{GS} decays from 3% to 0.9% of its initial value, while the rms magnetic field strength only falls from 67% to 63%, confirming that the magnetic field configuration approaches a GS equilibrium at $\sim t'_{\lambda B}$.

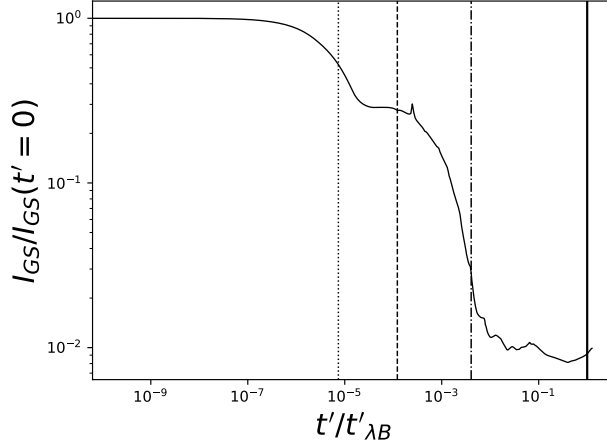


Figure 4.7: Time evolution of the “Grad-Shafranov integral” I_{GS} (defined in equation [4.10]). The vertical lines show, from left to right, the values of the time-scales $t'_{\zeta p}$, $t'_{\zeta g}$, $t'_{\zeta B}$, and $t'_{\lambda B}$.

4.2 Temperature evolution

4.2.1 Dependence on the artificial friction

In the previous simulations, we evolved the magnetic field but left the internal temperature constant. Now, we shall consider simulations where these two variables evolve and can affect each other. As a first step, we proceed to study the effects of the artificial friction on the thermal evolution. Evolving the temperature with the strategy proposed in Sec. 3.1, we found, for the same simulation we discussed in the Sec. 4.1.5, the results shown in panels (a) and (d) (pink

curve) in Fig. 4.8. These results can be understood by considering that the ratio between magnetic and thermal energy for a (non-superfluid) NS core is roughly (Reisenegger, 2009)

$$\frac{E_B}{E_T} \sim 1 \left(\frac{T}{10^{10}\text{K}} \right)^{-2} \left(\frac{B}{10^{16}\text{G}} \right)^2. \quad (4.11)$$

Thus, for this case, since we run the simulation for $b^2 = 0.03$ ($B \approx 3 \times 10^{17}$ G) and $T_0 = 3 \times 10^9$ K to evolve $\mathbf{B}(t')$, initially there is more magnetic than thermal energy, $E_B/E_T \sim 10^4$. This excess of magnetic energy is initially dissipated by the artificial friction \mathcal{L}_ζ , heating the core and increasing the neutrino equilibrium luminosity until $\mathcal{L}_\nu^* \approx \mathcal{L}_\zeta$ (at $\sim t_{\zeta B}$), then the temperature starts to decrease (at $\sim 10t_\lambda$). Therefore, the main effect of the artificial friction is to increase the internal temperature until $\mathcal{L}_\nu^* = \mathcal{L}_\zeta$, and then the passive cooling starts. One may see also that, due to the heating, the time-scales ratios $t_{\zeta p} : t_{\zeta g} : t_{\zeta B} : t_{\lambda B}$ are reduced with respect to the constant-temperature case, accelerating the evolution so the processes seem to happen almost at the same time ($\sim t_{\zeta B}$, see also Fig. 4.9).

The effect of the heating can be reduced by increasing the amount of initial thermal energy in the core. This can be achieved by starting with a higher T_0 in the simulations that evolve $\mathbf{B}(t')$, or by decreasing the magnetic field strength, but this is not numerically feasible (see Sec. 4.2.2). Once we set a value for $\zeta(T_0)$ (in this case 10^{-4}), running a simulation with a different initial temperature, kT_0 , in the t' variable is not expensive in terms of integration time because, as we are taking $\zeta = \zeta(T_0)(T/T_0)^{-6}$, all time-scales have the same temperature dependence and their ratios, $t'_{\zeta p} : t'_{\zeta g} : t'_{\zeta B} : t'_{\lambda B}$, remain unchanged but $\zeta(T_0)$ would differ by a factor k^{-6} ². Thus, we run two simulations to evolve $\mathbf{B}(t')$ with the same $b^2 = 0.03$, but with different (higher) initial temperatures, namely $T_0 = 3 \times 10^{10}$ K (with an initial ratio $E_B/E_T \sim 10^2$), and $T_0 = 10^{11}$ K (with an initial ratio $E_B/E_T \sim 10$). The results are shown in panels (b) and (d) (blue curve), and (c) and (d) (black curve), for each different initial temperature respectively. As we can see, comparing with the former results ($T_0 = 3 \times 10^9$ K), the effect of the initial heating is reduced because $\zeta(T_0)$ is a factor $(3 \times 10^{10}/3 \times 10^9)^{-6}$, and $(10^{11}/3 \times 10^9)^{-6}$ smaller. Hence, the same amount of magnetic energy is dissipated initially by the artificial friction, but during a much shorter time ($\sim t_{\zeta B}$). On the other hand, the initial equilibrium luminosity is also larger, so $\mathcal{L}_\nu^* \approx \mathcal{L}_\zeta$ on a shorter time also ($\sim t_{\zeta B}$) and the temperature increases less than in the former case. Sadly, our scheme makes the ratio $\mathcal{L}_\zeta/\mathcal{L}_{H\nu} \sim n_c^2/(\zeta\lambda L_c)$ temperature-independent during the long time-scales, and \mathcal{L}_ζ still dominates at these stages of the evolution even for a higher initial temperature. Nevertheless, since the effect of the initial heating is less significant, the time-scales are more separated (see Fig. 4.9), and we can see clearly how the magneto-thermal evolution proceeds: First, the star reaches the hydro-magnetic quasi-equilibrium at a time-scale $\sim t_{\zeta B}$, when the temperature

²In fact, running simulations with different T_0 is equivalent to take the results discussed in Sec. 4.1.5, and then apply the scaling $T(t') \rightarrow kT(k^{-6}t')$.

has not significantly evolved. Then, the core changes as a non-barotropic fluid at constant temperature until the time-scale $\sim 10t_\lambda$, when the temperature starts to decrease. And finally, as the core passively cools, it becomes barotropic as it approaches chemical equilibrium (at $\sim t_{\lambda B}$). This final process is slowed down with respect to the constant-temperature case because, as a result of the cooling, mUrca reactions operate less efficiently, delaying the approach to chemical equilibrium. In Fig. 4.9, one can easily see the delay by comparing the variables t' vs. t .

We remark that the chemical energy released, $\mathcal{L}_{H\nu}$, follows the expected evolution; it grows during the short time-scales ($< t_{\zeta B}$) reaching a maximum value that coincides with the maximum chemical imbalance (at $\sim t_{\zeta B}$). Then, it starts to decrease as the star approaches chemical equilibrium, and also due to the cooling (see the upper panels (b), and (c), in Fig. 4.8). This last effect is the main difference with the constant temperature case, and can be seen also in \mathcal{L}_ζ since it has the same temperature dependence. In Sec. 4.2.3, we shall discuss whether $\mathcal{L}_{H\nu}$ can play a significant role in the thermal evolution for different parameters.

Finally, we remark that the initial heating is expected because \mathcal{L}_ζ dominates the short-term evolution and represents the energy dissipated by Alfvén waves due to the readjustment of the magnetic field. Nevertheless, our model only mimics the short-term dynamics of the order of an associated Alfvén crossing time, but does not solve it correctly, so the heating is only qualitatively correct.

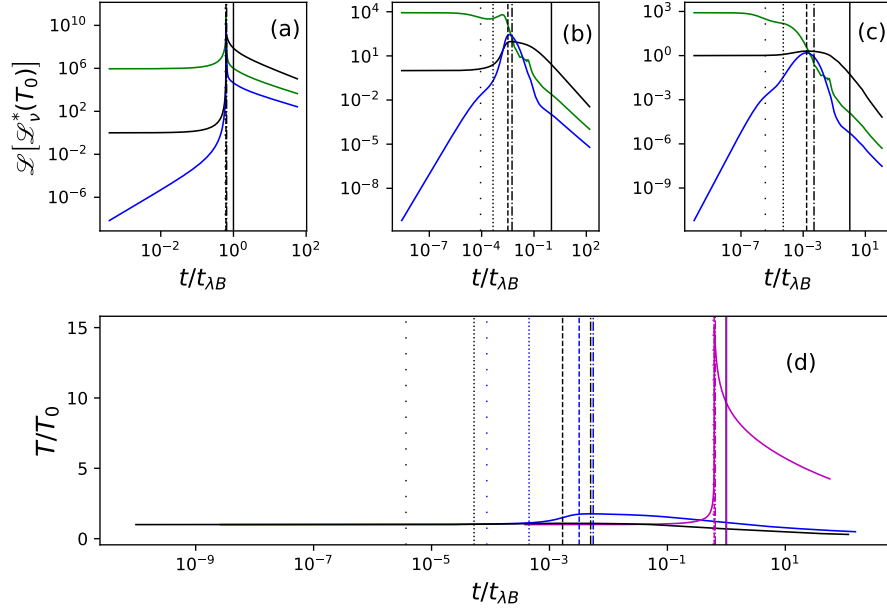


Figure 4.8: Thermal evolution: The upper panels show the luminosities for the artificial friction dissipation \mathcal{L}_ζ (green), chemical energy released $\mathcal{L}_{H\nu}$ (blue), and equilibrium neutrino luminosity \mathcal{L}_ν^* (black), normalized to the initial value $\mathcal{L}_\nu^*(t=0)$. Panel (a) corresponds to the thermal evolution for the simulation discussed in Sec. 4.1.5, where the initial temperature is $T_0 = 3 \times 10^9$ K. Panels (b) and (c) correspond to the simulations with $T_0 = 3 \times 10^{10}$ K, and $T_0 = 10^{11}$ K, with different values of $\zeta(T_0)$ ($10^{-4} \times [3 \times 10^{10}/3 \times 10^9]^{-6} = 10^{-10}$ and $10^{-4} \times [10^{11}/3 \times 10^9]^{-6} = 7.3 \times 10^{-14}$, respectively). Panel (d) shows the evolution of temperature, normalized to T_0 , for each of the former values; the pink curve corresponds to the results shown in panel (a), the blue curve to panel (b), and the black curve to panel (d). For all these simulations, the magnetic field strength was the same $B \approx 3 \times 10^{17}$ G ($b^2 = 0.03$). The vertical lines show, from left to right, the values of the time-scales $t_{\zeta p}$, $t_{\zeta g}$, $t_{\zeta B}$, t_λ , and $t_{\lambda B}$, obtained from equation (3.9).

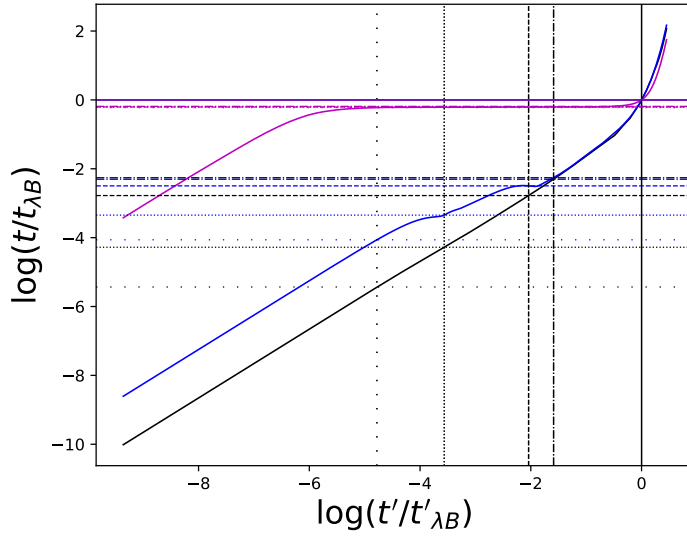


Figure 4.9: Time variable comparison between the constant-temperature variable t' and the variable-temperature time variable t . The curves correspond to the same simulations shown in Fig. 4.8: In pink, the results in panel (a) (pink curve also in panel (d)); in blue, the results in panels (b) (blue curve also in panel (d)); and in black the results in panels (c) (black curve also in panel (d)), and (f). The horizontal lines, for each color and from bottom to top, correspond to the time-scales $t_{\zeta p}$, $t_{\zeta g}$, $t_{\zeta B}$, t_{λ} , and $t_{\lambda B}$ (obtained from equation [3.9]), with their respective colors. The vertical lines, for each color and from left to right, correspond to $t'_{\zeta p}$, $t'_{\zeta g}$, $t'_{\zeta B}$, t'_{λ} and $t'_{\lambda B}$.

4.2.2 Magnetic field scaling

So far, we have used typical values of the internal temperature under which the strong-coupling regime operates. However, due to the unrealistic high magnetic field strength we used, $B \approx 3 \times 10^{17}$ G, the magneto-thermal evolution is very fast since $t_{\lambda B} \propto B^{-2}$ (see Fig. 4.10). Even for magnetars, the externally observed dipole magnetic field strength is only $B \sim 10^{14-15}$ G. However, it has been speculated that internal toroidal fields might be much stronger than the externally detectable poloidal dipole (Thompson & Duncan, 2001; Shabaltas & Lai, 2012; Gotthelf et al., 2013). In fact, assuming only the mUrca passive cooling (equation [2.55]), one can show that the internal magnetic field strength must be at least of order $B \sim 10^{16}$ G, so that there is enough magnetic energy to sustain a hot core over the typical magnetar age $\tau \sim 10^{11}$ s (Beloborodov & Li, 2016). In our numerical scheme, using a smaller field is expensive in terms of integration time. Therefore, since we are interested only in the results around $\sim t_{\lambda B}$, we performed the scaling (before evolving the temperature)

$$\mathbf{B}(t') \rightarrow k\mathbf{B}(k^{-2}t') \quad (4.12)$$

to the results we already have, so that the magnetic field strength is now smaller. To test this scaling, we run two simulations with modestly small values of b^2 in the variable t' . The results, after evolving the temperature, are shown in Fig. 4.10, where in panels (c) and (d) we scaled the curves for $\mathcal{L}_{H\nu}$ and \mathcal{L}_{ζ} , with values of $b^2 = 0.02$ and 0.03 , to the results with $b^2 = 0.01$. As one can see, this procedure works fairly well for the time-scales in which we are interested. This is expected because the results scale with B for time-scales $t > t_{\zeta B}$, when the hydromagnetic quasi-equilibrium is reached and the pressure forces balance the Lorentz force. In the following section we shall use this scaling for a more realistic field. Here and hereafter, we present the results in physical units instead of code units to remark how fast the thermal evolution is for the values of B and T_0 we have used. In fact, for $B \approx 3 \times 10^{11}$ G and $T_0 = 10^{11}$, the sound crossing time t_{cs} ($\sim t_{\zeta g}$) is even smaller than t_{λ} . Therefore, the results we presented in this entire section are not physically correct but illustrative to understand how our numerical approach works. This problem shall be solved in the following section by taking a smaller magnetic fields strength using this scaling.

4.2.3 Magnetic feedback

Now we focus on answering whether the curves for $\mathcal{L}_{H\nu}$ and \mathcal{L}_{ν}^* will intersect at some point in time, leading to a possible magnetic feedback on the evolution of the temperature. To answer this question, we may use equations (2.57), (2.65), and (2.66), so the square root of the ratio between the chemical energy released and the equilibrium luminosity is roughly

$$\sqrt{\frac{\mathcal{L}_{H\nu}}{\mathcal{L}_{\nu}^*}} \sim \sqrt{\xi H(\xi < 3)} \sim 0.4 |\xi|. \quad (4.13)$$

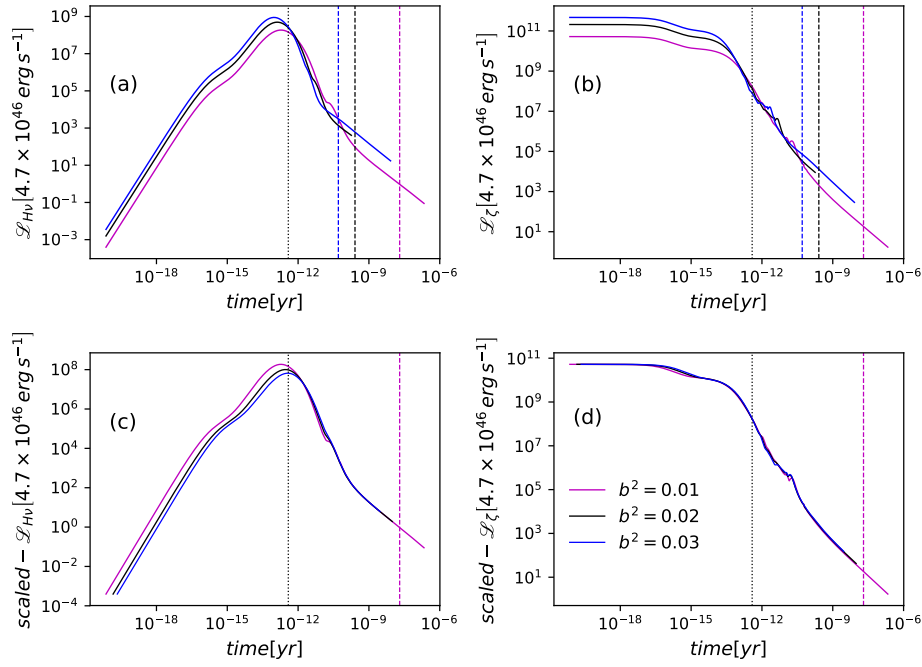


Figure 4.10: Magnetic field scaling: The upper panels, (a) and (b), show the curves for the chemical energy released $\mathcal{L}_{H\nu}$, and the artificial friction dissipation \mathcal{L}_ζ after evolving temperature with $T_0 = 10^{11}$ K, and three different values of b^2 (0.01, pink; 0.02, black; and 0.03, blue). The lower panels (c) and (d), show the same curves after applying the scaling in equation (4.12), to the results with $b^2 = 0.02$ and 0.03 , to obtain the results with $b^2 = 0.01$. The vertical lines correspond, from left to right, t_λ and $t_{\lambda B}$ (with their respective colors in the upper panels), obtained from equation (3.9).

Therefore, if $|\xi| \gtrsim 1$, then $\mathcal{L}_{\text{H}\nu} \gtrsim \mathcal{L}_\nu^*$ and the magnetic feedback in the internal temperature evolution can occur. Thus, by replacing the transition temperature from the “strong-coupling” to the “weak-coupling regime”, T_{eq} (equation [2.69]), into the condition $\Delta\mu/k_B T > 1$ with $\Delta\mu \sim B^2/4\pi n_c$, we obtain the minimum magnetic field strength for which the magnetic feedback can occur, namely

$$B_{\text{MF}} \gtrsim 3 \times 10^{15} \text{G}. \quad (4.14)$$

In Fig. 4.11, we show the results after evolving the temperature for a scaled magnetic field strength $B \approx 0.28 \times (3 \times 10^{17} \text{G}) \approx 8 \times 10^{16} \text{G}$, and with $T_0 = 10^{11} \text{K}$. In panel (a), we see that the temperature decreases further below T_{eq} , so beyond that point we cannot trust the simulation results. Panel (b) shows a non-physical magnetic feedback because $\mathcal{L}_\zeta = \mathcal{L}_\nu^*$ at late times, where \mathcal{L}_ζ is affected by the lack of numerical accuracy discussed in Sec. 4.1.4. It can also be seen that this happens in the unphysical regime when the core is already in the “weak-coupling regime”. Panel (c) shows the evolution of ξ , and $\sqrt{\mathcal{L}_{\text{H}\nu}/\mathcal{L}_\nu^*}$, which is roughly the same for both variables as we have just discussed. We see also that the condition $|\xi| > 1$ is never fulfilled, and the non-physical feedback affects ξ and $\sqrt{\mathcal{L}_{\text{H}\nu}/\mathcal{L}_\nu^*}$ in the final stages. Thus, although one can estimate a minimum magnetic field strength, equation (4.14), for which the magnetic feedback is possible, our results show that it does not occur at temperatures larger than T_{eq} . This is a general conclusion because, since $\mathcal{L}_{\text{H}\nu} \propto B^4$, for smaller magnetic field strength the equilibrium neutrino luminosity would intersect $\mathcal{L}_{\text{H}\nu}$ at even smaller temperatures. Therefore, the magnetic feedback on the core temperature, due to non-equilibrium mUrca reactions, is very unlikely for young magnetars.

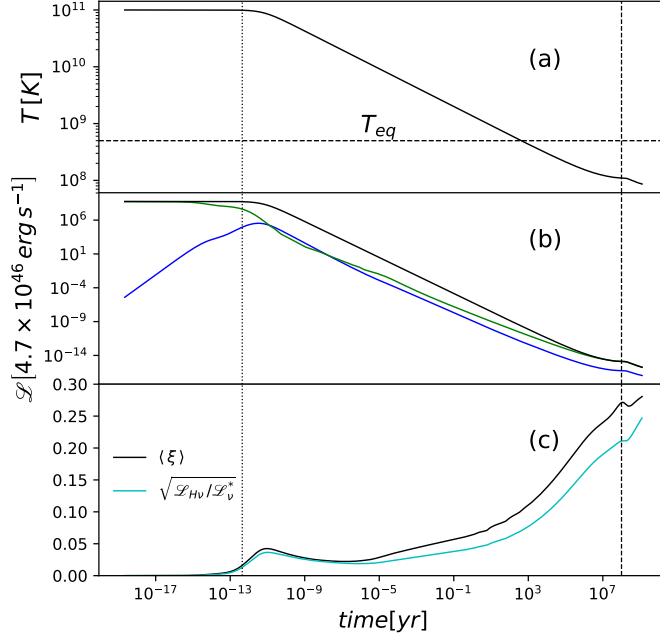


Figure 4.11: Magneto-thermal evolution: In panel (a), the evolution of temperature with $T_0 = 10^{11}$ K, and the horizontal line corresponds to $T_{eq} = 5 \times 10^8$ K (defined in equation [2.69]), where the transition to the weak-coupling regime occurs and the present approach ceases to be valid. Panel (b) shows the equilibrium neutrino luminosity \mathcal{L}_ν^* (black), chemical energy released $\mathcal{L}_{H\nu}$ (blue), and the artificial friction dissipation \mathcal{L}_ζ (green). Panel (c) shows the evolution of $\langle \xi \rangle$ (black), and $\sqrt{\mathcal{L}_{H\nu}/\mathcal{L}_\nu^*}$ (cyan), where $\langle . \rangle$ denotes root mean square (rms) average in the volume of the core. The vertical lines correspond, from left to right, to t_λ and $t_{\lambda B}$, obtained from equation (3.9). Here the magnetic field strength has been scaled, using equation (4.12), from $B \approx 3 \times 10^{17}$ G ($b^2 = 0.03$) to $B \approx 8 \times 10^{16}$ G ($b^2 = 0.002$).

Chapter 5

Conclusion

For a young magnetar, the particle species in the core move together since they are strongly coupled by collisions and convert into each other by weak interactions (mUrca reactions). As the star passively cools due to neutrino emission, the magnetic field induces small fluid displacements changing the local chemical composition, leading to an enhancement of the neutrino luminosity and releasing thermal energy in the core. Depending on the strength of the chemical imbalance, a magnetic feedback on the thermal evolution is possible, and can be either a stronger cooling (if $\xi \approx 1 - 5$) or a net heating (if $\xi > 5$). In this thesis, we have deeply studied the magneto-thermal evolution in the “strong-coupling regime”, including the possibility of a magnetic feedback on the thermal evolution as a consequence of the magnetic field decay. The results can be summarized as follows:

1. Constant temperature:

- (i) In the “weak-coupling regime”, [Castillo et al. \(2020\)](#) used the artificial friction method to reach (and then maintain) the hydro-magnetic quasi-equilibrium, leading to the same kind of non-barotropic “twisted torus” quasi-equilibrium previously found in MHD simulations [Braithwaite & Spruit \(2004\)](#); [Braithwaite \(2006\)](#) in the Alfvén-like crossing time-scale $t'_{\zeta B}$. Here, we have corroborated the effectiveness of this method for the “strong-coupling regime”.

- (ii) Each of the physical processes associated with the time-scales $t_{\zeta p}$, $t_{\zeta g}$, and $t_{\zeta B}$, are found to be in good agreement. The long-term evolution of the magnetic field is not significantly affected by the artificial friction force if the ratio between the energy it dissipates and the chemical energy released, $\mathcal{L}_{\zeta}/\mathcal{L}_{H\nu}$, is small enough, which imposes an upper bound on $\zeta(T_0)$ given in equation (2.78). However, although our simulations satisfy this condition, the final value of $\mathcal{L}_{\zeta}^{\text{Tor}}$ is affected by a problem of numerical accuracy since the latter is obtained from the cross product of two nearly parallel vectors, $\nabla\alpha$ and $\nabla\beta$. Therefore, our numerical scheme needs to be improved in order to solve this issue.

2. Variable temperature:

(i) The strategy we introduced allowed us to easily include the temperature evolution. The effect of the artificial friction only modifies the temperature at which the passive cooling starts (when $\mathcal{L}_\zeta = \mathcal{L}_\nu^*$), and can be neglected if initially there is more thermal than magnetic energy in the core.

(ii) During the early life of a magnetar, the possibility of a magnetic feedback in the star's thermal history, due to non-equilibrium mUrca reactions, is in principle possible for internal magnetic fields strength $B_{\text{MF}} \gtrsim 3 \times 10^{15} \text{G}$. However, our results show that this does not occur because the star quickly reaches the “weak-coupling regime” ($\sim 10^2 \text{yr}$), so the feedback would proceed for lower temperatures when most of the magnetic energy is dissipated by ambipolar diffusion.

Bibliography

- Akmal A., Pandharipande V., Ravenhall D., 1998, [PhysRevC](#), **58**, 1804
- Baade W., Zwicky F., 1934, [PhysRev](#), **46**, 76
- Baym G., Pethick C., Pikes D., 1969, [Nature](#), **224**, 674
- Beloborodov A. M., Li X., 2016, [ApJ](#), **833**, 261
- Bonanno A., Urpin V., Belvedere G., 2005, [A&A](#), **440**, 199
- Braithwaite J., 2006, [A&A](#), **449**, 451
- Braithwaite J., Spruit H. C., 2004, [Nature](#), **431**, 819
- Burrows A., Lattimer J. M., 1986, [ApJ](#), **307**, 178
- Castillo F., Reisenegger A., Valdivia J. A., 2017, [MNRAS](#), **471**, 507
- Castillo F., Reisenegger A., Valdivia J. A., 2020, [MNRAS](#), **498**, 3000
- Chadwick J., 1932, [Nature](#), **129**, 312
- Chakrabarty D., Pivovarov M. J., Hernquist L. E., Heyl J. S., Narayan R., 2001, [ApJ](#), **548**, 800
- Chiu H.-Y., Salpeter E. E., 1964, [PhysRevLett.](#), **12**, 413
- Cruces M., Reisenegger A., Tauris T. M., 2019, [MNRAS](#), **490**, 2013
- Cumming A., Arras P., Zweibel E., 2004, [ApJ](#), **609**, 999
- Cumming A., Brown E. F., Fattoyev F. J., Horowitz C., Page D., Reddy S., 2017, [PhysRevC](#), **95**, 025806
- Duncan R. C., Thompson C., 1992, [ApJ](#), **392**, L9
- Durant M., van Kerkwijk M. H., 2006, [ApJ](#), **650**, 1070
- Friman B. L., Maxwell O. V., 1979, [ApJ](#), **232**, 541
- Glen G., Sutherland P., 1980, [ApJ](#), **239**, 671

- Goldreich P., Reisenegger A., 1992, *ApJ*, **395**, 250
- Gotthelf E. V., Halpern J. P., Alford J., 2013, *The Astrophysical Journal*, 765, 58
- Gourgouliatos K. N., Cumming A., 2014, *PhysRevLett.*, 112, 171101
- Grad H., Rubin H., 1958, *Journal of Nuclear Energy (1954)*, 7, 284
- Gusakov M. E., Kantor E. M., 2013, *PhysRevD*, 88, 101302
- Gusakov M., Kantor E., Ofengeim D., 2017, *PhysRevD*, 96, 103012
- Haensel P., 1992, *A&A*, **262**, 131
- Haensel P., Levenfish K. P., Yakovlev D. G., 2002, *A&A*, **394**, 213
- Hewish A., Bell S. J., Pilkington J. D., Scott P. F., Collins R. A., 1968, *Nature*, **217**, 709
- Ho W., 2012, *PIAU*, 8
- Hoyos J., Reisenegger A., Valdivia J., 2008, *A&A*, **487**, 789
- Kaplan D. L., Van Kerkwijk M., 2005, *ApJ*, 628, L45
- Kaplan D. L., Van Kerkwijk M., 2009, *ApJ*, 705, 798
- Kaspi V. M., 2010, *PNAS*, **107**, 7147
- Kaspi V. M., McLaughlin M. A., 2004, *ApJ*, 618, L41
- Keane E. F., Kramer M., 2008, *MNRAS*, 391, 2009
- Keil W., Janka H. T., 1995, *AaP*, **296**, 145
- Levenfish K., Yakovlev D., 1994, *Astron. Rep.*, **38**, 247
- Manchester R. N., Hobbs G. B., Teoh A., Hobbs M., 2005, *AJ*, 129, 1993
- McLaughlin M. A., et al., 2006, *Nature*, 439, 817
- Mereghetti S., Tiengo A., Israel G. L., 2002, *ApJ*, 569, 275
- Mereghetti S., Pons J. A., Melatos A., 2015, *SSRv*, **191**, 315
- Ofengeim D. D., Gusakov M. E., 2018, *PhysRevD*, 98, 043007
- Olausen S. A., Kaspi V. M., 2014, *ApJS*, **212**, 6
- Pavlov G. G., Luna G. J. M., 2009, *ApJ*, 703, 910
- Pethick C. J., 1992, in *Structure and Evolution of Neutron Stars*. p. 115
- Pons J., Viganò D., 2019, *Living Rev Comput Astrophys*, 5

- Pons J. A., Reddy S., Prakash M., Lattimer J. M., Miralles J. A., 1999, *ApJ*, 513, 780
- Prendergast K. H., 1956, *ApJ*, 123, 498
- Rea N., 2014, *AN*, 335, 329
- Reisenegger A., 1995, *ApJ*, 442, 749
- Reisenegger A., 2009, *A & A*, 499, 557
- Shabaltas N., Lai D., 2012, *The Astrophysical Journal*, 748, 148
- Shafranov V. D., 1966, *Reviews of Plasma Physics*, 2, 103
- Shapiro S. L., Teukolsky S. A., 1983, New York: John Wiley & Sons
- Spruit H. C., 2009, *PIAU*, 4, 61
- Thompson C., Duncan R. C., 1993, *ApJ*, 408, 194
- Thompson C., Duncan R. C., 1995, *MNRAS*, 275, 255
- Thompson C., Duncan R. C., 1996, *ApJ*, 473, 322
- Thompson C., Duncan R. C., 2001, *The Astrophysical Journal*, 561, 980
- Thorne K. S., 1977, *ApJ*, 212, 825
- Weltevrede P., Stappers B. W., Rankin J. M., Wright G. A. E., 2006, *ApJ*, 645, L149
- Woltjer L., 1964, *ApJ*, 140, 1309
- Yakovlev D. G., Pethick C., 2004a, *ARA & A*, 42
- Yakovlev D., Pethick C., 2004b, *ARAA*, 42, 169
- Yakovlev D., Shalybkov D., 1990, *SvA Lett*, 16, 86